Robust energy harvesting from walking vibrations by means of nonlinear cantilever beams

Citation: Kluger, Jocelyn M., Themistoklis P. Sapsis, and Alexander H. Slocum. "Robust Energy Harvesting from Walking Vibrations by Means of Nonlinear Cantilever Beams." Journal of Sound and Vibration 341 (2015): 174–194.

As Published: http://dx.doi.org/10.1016/j.jsv.2014.11.035

Publisher: Elsevier

Persistent URL: http://hdl.handle.net/1721.1/108080

Version: Author's final manuscript: final author's manuscript post peer review, without publisher's formatting or copy editing

Robust energy harvesting from walking vibrations by means of nonlinear cantilever beams

Jocelyn M. Kluger, Themistoklis P. Sapsis*, Alexander H. Slocum

Department of Mechanical Engineering, Massachusetts Institute of Technology
77 Massachusetts Ave, Cambridge MA 02139

Abstract

In the present work we examine how mechanical nonlinearity can be appropriately utilized to achieve strong robustness of performance in an energy harvesting setting. More specifically, for energy harvesting applications, a great challenge is the uncertain character of the excitation. The combination of this uncertainty with the narrow range of good performance for linear oscillators creates the need for more robust designs that adapt to a wider range of excitation signals. A typical application of this kind is energy harvesting from walking vibrations. Depending on the particular characteristics of the person that walks as well as on the pace of walking, the excitation signal obtains completely different forms. In the present work we study a nonlinear spring mechanism that is comprised of a cantilever wrapping around a curved surface as it deflects. While for the free cantilever, the force acting on the free tip depends linearly with the tip displacement, the utilization of a contact surface with the appropriate distribution of curvature leads to essentially nonlinear dependence between the tip displacement and the acting force. The studied nonlinear mechanism has favorable mechanical properties such as low frictional losses, minimal moving parts, and a rugged design that can withstand excessive loads. Through numerical simulations we illustrate that by utilizing this essentially nonlinear element in a 2 degrees-of-freedom (DOF) system, we obtain strongly nonlinear energy transfers between the modes of the system. We illustrate that this nonlinear behavior is associated with strong robustness over three radically different excitation signals that correspond to different walking paces. To validate the strong robustness properties of the 2DOF nonlinear system, we perform a direct parameter optimization for 1DOF and 2DOF linear systems as well as for a class of 1DOF and 2DOF systems with nonlinear springs similar to that of the cubic spring that are physically realized by the cantilever-surface mechanism. The optimization results show that the 2DOF nonlinear system presents the best average performance when the excitation signals have three possible forms. Moreover, we observe that while for the linear systems the optimal performance is obtained for small values of the electromagnetic damping, for the 2DOF nonlinear system optimal performance is achieved for large values of damping. This feature is of particular importance for the the system's robustness to parasitic damping.

Keywords: Nonlinear cantilever beam; Energy harvesting; Robustness to uncertain excitation; Targeted energy transfer; Nonlinear vibrations; Robustness to parasitic damping

1. Introduction

Several technological processes such as energy harvesting from ambient vibrations, shock absorption from external loads, and passive control or suppression of mechanical instabilities involve targeted energy transfer from one component of a structure to another. In particular, energy harvesting is the process of using ambient energy sources to generate useful forms of energy such as electricity. The energy in these ambient sources is usually spread over a range of frequencies. Applications of energy harvesting range from MEMs sensors implanted in the human body to monitor biological signs, von Büren et al. [1], to small electronics such as wireless sensors in remote locations, Paradiso and Starner [2]. Shock absorption is the process of protecting a primary structure from an ambient force or external pressure load. Applications of shock absorption include passive protection of buildings from earthquake excitations, of offshore platforms from water wave impacts, and of delicate instruments from external loads, as studied by Manevitch et al. [3], Vakakis et al. [4], and Sapsis et al. [5]. Passive control of mechanical instabilities is another important area that has recently emerged in the context of targeted energy transfer. Examples include the suppression of aeroelastic instabilities on wings due to fluttering, Lee et al. [6], and the elimination of aeroelastic instabilities in suspension bridges, Vaurigaud et al. [7].

In all of these cases, one aims to design elements that are capable of transferring the energy irreversibly and efficiently. In typical applications (especially energy harvesting), the ambient vibration can be described as a stochastic, multi-frequency signal that is often characterized by time-varying features, Stanton et al. [8]. However, traditional single degree of freedom linear vibration harvesters are efficient only close to their design point; that is, when the excitation frequency matches the harvester's natural frequency. Therefore, linear harvesters respond inefficiently to vibrations with uncertain characteristics, Tang and Zuo [9]. In order to absorb ambient vibrations effectively, it is essential for an energy harvester to be characterized by performance robustness when the excitation signal has radically different properties over time.

Below, we give an overview of methods for overcoming the excitation mistuning problem. Then, we discuss some mechanical challenges to designing ambient vibration oscillators, and the importance of an oscillator design that can overcome both the excitation mistuning problem and these mechanical challenges.

Methods for overcoming the mistuning problem include: designing systems that do not use a spring, control theory of linear spring systems, two-degree-of-freedom linear systems, continuous linear systems, and nonlinear springs.

Devices that oscillate without a spring do not have resonant frequencies and respond similarly to acceleration signals that have similar magnitudes but different frequencies. For example, Mitcheson et al. [10]

*Corresponding author: sapsis@mit.edu, Tel: +1 617-324-7508, Fax: +1 617-253-8689

describe a micro-scale coulomb-force parametric generator (CFPG). Instead of using a spring, the CFPG uses a charged capacitor plate that snaps away from a counter-electrode when excited by large accelerations. The CFPG, however, only functions well when the excitation displacement greatly exceeds the allowable travel length of its sliding plate. Another shock absorption device that functions without a spring is the MEMS-fabricated hydraulic valve that fits inside a shoe, as described by Yaglioglu [11]. In this device, a controller allows hydraulic fluid flowing in between two chambers to pulse on a piezoelectric element. Resulting strain in the piezoelectric element converts the mechanical energy into electric energy. Additionally, Paradiso and Starner [2] discuss a device small enough to fit in a shoe that consists of a clam shell made from two piezoelectric elements that flattens with each heel-strike. Paradiso and Starner also review other energy harvesting devices that absorb ambient energy without vibrating [2].

The performance (i.e. peak power output, adaptivity, and robustness to varied excitations) of energy harvesters with linear springs can be improved by using control strategies to alter the oscillator's resonant frequency, as described by Tang and Zuo [9], or creating linear devices with two or more degrees of freedom so that they have multiple resonant frequencies, as described by Trimble in [12]. [9] and [12] both present devices with better performance than traditional 1DOF linear systems. Some general drawbacks of these devices, however, are that the controlled devices consume some of the collected power, and the multiple degree of freedom systems are bulky and have limited robustness.

Another approach is to use a nonlinear spring. Essentially nonlinear springs (that is nonlinear springs without linear stiffness components) do not have preferential linear frequencies. Therefore, they are more robust to variations in the external excitation and preserve their good performance level for a wide range of conditions, as described in Vakakis et al. [4], Gendelman et al. [13], Sapsis et al. [14], and Quinn et al. [15]. The simplest form of an essentially nonlinear spring is a cubic one. One way to implement a cubic spring is by linear springs supporting the proof mass at various angles to its direction of travel. For example, MacFarland et al. [16] investigate the dynamics of a nonlinear oscillator realized by a thin elastic rod (piano wire) clamped at its ends without pretension that performs transverse vibrations at its center. To leading order approximation, the stretching wire produces a cubic stiffness nonlinearity. The effectiveness of this design has been illustrated for energy harvesting applications from impulsive excitations in [17, 18].

Similarly, Hajati et al. [19] describe an ultra-wide bandwidth resonator made out of a doubly-clamped piezoelectric beam. The double-clamps cause the cantilever to stretch as it bends, resulting in a nonlinear stiffness. As described by Freeman [20], nonlinear springs may also be physically implemented by helical coil springs with thickening coil wires or changing overall diameters. Another way to achieve nonlinear behavior is by employing multiple linear components that interact more strongly the further they deflect. For example, in the leaf springs of automobile suspensions, several layers of arc-shaped spring steel are clamped together. As the center of the upper arc deflects, it contacts the arc below it, and both springs further deflect in contact. As more and more arcs deflect, the spring effectively stiffens [20].

A different class of nonlinear springs are those with negative linear stiffnesses, which are usually characterized by bi-stable configurations. Cottone et al. [21] describe a nonlinear spring implemented by an inverted pendulum with a tip magnet that faces an opposing static magnet. For a small enough gap between the magnets, the cantilever has two equilibria. For small base input accelerations, the tip magnet oscillates linearly about one of the equilibria. For sufficiently large accelerations, the tip magnet cycles between the two equilibria. This resonance is insensitive to noise.

Mann and Sims [22] describe an oscillator that is implemented by a magnet sliding in a tube with two opposing magnets as the end caps. This configuration causes the stiffness to be the summation of a linear and cubic component. While linear stiffness hinders the system's adaptivity and robustness to different excitation spectra, Carrella et al. [23] describe how the effective linear stiffness component can be reduced by counteracting it with a negative stiffness component using magnets arranged in an attracting configuration. In another study, Kovacic et al. [24] demonstrate that a negative stiffness can be implemented using oblique pre-stressed springs.

The goal of this work is the development of a nonlinear 2DOF system that will be able to maintain its good energy harvesting performance over a wide range of input signals. To achieve this goal we plan to utilize mechanical nonlinearities that will be chosen so that conditions for targeted energy transfers between modes are realized. To implement the desired nonlinearity we propose the use of a cantilever beam that oscillates between two contact surfaces with carefully selected curvature. For the purposes of energy harvesting, the proposed design has many desired properties which we illustrate analytically, numerically, and experimentally. These properties include i) the resulting nonlinear spring has a negligible linearized component, ii) the order of its nonlinearity does not remain constant but increases as the amplitude gets larger, and iii) the spring achieves a theoretically infinite force for a finite displacement. The last property is of crucial importance since it allows the device to act as a typical nonlinear spring (with polynomial nonlinearity) for moderate vibration amplitudes and to effectively behave as a vibro-impact spring for larger amplitudes, which protects the device from excessive accelerations. After we have developed and studied the nonlinear element, we proceed with a thorough numerical study that illustrates clearly the advantages of the 2DOF nonlinear energy harvester compared to 1DOF designs and 2DOF linear systems. More specifically, focusing on the energy harvesting challenge of walking vibrations, we collect three radically different excitation signals that correspond to three different human body motions (walking, walking quickly, running). For each family of systems we perform an optimization of system parameters, after which we conclude that the 2DOF energy harvester has almost double average harvested power compared with the 1DOF systems and the 2DOF linear system. In addition, we observe that while the linear system's optimal performance is obtained for small values of the electromagnetic damping, the 2DOF nonlinear system optimal performance is achieved for large values of damping. This feature is of particular importance for the the system's robustness to parasitic damping.

2. Essentially nonlinear springs based on cantilever beams and contact surfaces

The new nonlinear element is based on a cantilever beam that oscillates between two surfaces of given geometry (i.e. distribution of curvature). In particular, it is a modification of Timoshenko's design that consists of a cantilever that wraps along a surface as it bends (Fig. 1) [25]. Other modifications of Timoshenko's design are described in Freeman [20], Li [26], and Li et al. [27]. This general design has the favorable mechanical properties of low friction (the cantilever only slides a small amount along the surface), only one moving part (which increases fatigue lifetime), and surfaces that prevent excessive deflection (which protects the cantilever from yielding).

Timoshenko investigated a spring for which the surface has a constant radius of curvature (i.e. a quadratic shape). In this case the cantilever-quadratic-surface spring behaves linearly until a critical force is applied (see below for details). Above the critical force, the cantilever-quadratic-surface spring behaves nonlinearly. However, during the initial regime (whose extent cannot be reduced), the spring resonates primarily with a single dominant frequency and therefore it suffers from the usual disadvantages that characterize linear systems such as lack of adaptivity to different excitation spectra and lack of power robustness to varied excitations.

In contrast to a contact surface with a constant curvature, this paper employs a contact surface with variable curvature along its length and demonstrates that this modification can substantially change the behavior of the nonlinear element. It is well known that the behavior of a free cantilever tip is linear for small displacements or forces, and the cantilever radius of curvature is smallest (roundest) at the root and infinite (straight beam) at the tip. For this reason, the surface radius of curvature is made infinite at the cantilever's root and decreasing along its length. That is, the second derivative of the surface spatial function equals zero at the root and grows larger along the length. Accordingly, contact between the beam and the surface begins immediately after the application of even a very small force.

As proven in this section, this choice in surface curvature eliminates the linear regime that characterizes the original Timoshenko design and leads to essentially nonlinear behavior of the element. As described by Remick et al. [17, 18] for the case of impulsive excitation, and demonstrated in the next section of this paper for continuous excitation with variable characteristics, the use of completely nonlinear springs in multi-degree-of-freedom oscillators greatly increases the system's adaptivity to different excitations (i.e. its ability to adjust its resonance frequency/ies depending on the input spectrum). This adaptivity is related to the strong energy transfer between nonlinear modes, a phenomenon that only occurs in the presense of suitably selected nonlinearity. This nonlinear energy transfer is greatly reduced if the springs have linear regimes. Therefore modifying Timoshenko's spring to remove the linear regime is a key adjustment to the design.

The force versus deflection relationship of both Timoshenko's original design and the proposed one follow

the same general derivation given below. The schematic for both nonlinear springs is shown in Fig. 1. In the original Timoshenko design for a surface with a constant radius of curvature, the surface shape has the form:

$$S = D\left(\frac{z}{L_{\text{Surf}}}\right)^2 = \frac{z^2}{2R} \tag{1}$$

where $D = L_{\text{Surf}}^2/2R$ is the gap between the surface and undeflected cantilever at the end of the surface ($z = L_{\text{Surf}}$). R is the surface constant radius of curvature ($1/R = \mathrm{d}^2S/\mathrm{d}z^2$), and z is the coordinate in the axial direction along the surface. In our modified design, the surface shape is given the form:

$$S = D\left(\frac{z}{L_{\text{Surf}}}\right)^n \tag{2}$$

where D, L_{Surf}, and z are defined in the same way as in Eq. (1). n is an arbitrary power greater than 2. For reasons described below and in Section 2.1, this constraint on n ensures that the spring is essentially nonlinear.

Generally speaking, both Timoshenko's original spring and our modified spring behave nonlinearly because longer lengths of the cantilever wrap along the surface as more force is applied. When additional force is applied, additional deflection of the entire spring is due to deflection on the free cantilever length that is not wrapped along the surface. Therefore, as the free cantilever's length shortens and the free cantilever becomes stiffer (shorter), the entire spring stiffens.

For reasons described in Section 2.1, we require $n \geq 2$ for the cantilever to increasingly contact the surface and cause the spring stiffen as more force is applied. When $n = 2$ (a surface with constant curvature), the cantilever deflects a certain amount before contacting the surface. When $n > 2$ (a surface with 0 curvature at its root and increasing curvature along its length), any small force causes cantilever-surface contact and therefore spring stiffening. If $n < 2$, the cantilever does not contact the surface, and consequently the spring remains linear. The theory applies when n is any real number, not just an integer. When n is not an integer, its behavior is a hybrid of the two closest integer values.

This section will discuss the effect of varied n values on the spring nonlinear behavior. First, we derive the theory for the spring deflection as a function of the applied force, which is closely related to the cantilever-surface contact point, z_c. Then, we describe the effect of varied parameter values, such as the surface-cantilever end gap D, cantilever rigidity EI, length L, and particularly n, on the cantilever-surface contact point, deflection, and spring stiffness as function of the applied force. We also describe the stress in the cantilever, which is useful for preventing material yield in the spring. Finally, we fabricate a spring and experimentally verify the nonlinear static force-deflection curve and nonlinear dynamics.

First, we derive the nonlinear spring theory. The deflection of the cantilever tip, y can be approximated as the sum of three components:

$$y = \delta_1 + \delta_2 + \delta_3 \tag{3}$$

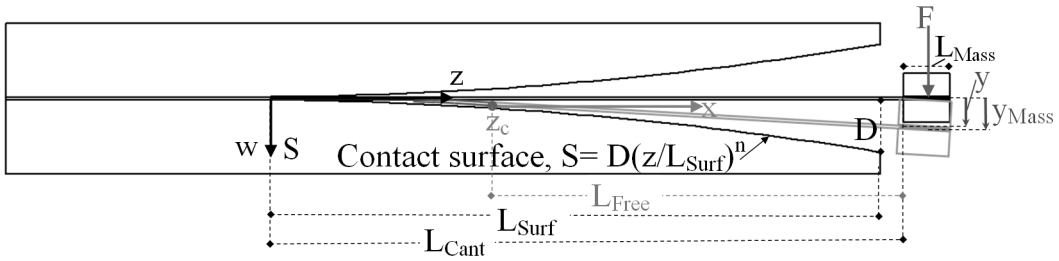

Figure 1: Nonlinear spring implemented by a cantilever beam that vibrates between two curved surfaces. The cantilever has length L_{Cant}, second moment of area I, and elastic modulus E. The surface curve has the form $S = D(z/L_{\text{Surf}})^n$, where D is the gap between the surface end and undeflected cantilever, and n is an arbitrary power greater than 2. The axial coordinate z is measured from the surface root. The axial coordinate x is measured from the contact point, z_c. The cantilever deflects in the w direction. Deflection at the cantilever tip is labeled y and deflection at the mass tip is labeled y_{Mass}.

The first component, δ_1, is the displacement of the "free" part of the cantilever (L_{Free} in Fig. 1),due to bending. The tip displacement of this beam segment is found using the Euler-Bernoulli equation:

$$EI\frac{\mathrm{d}^4 w}{\mathrm{d}x^4} = -q(x) \tag{4}$$

where x is the axial coordinate measured from the contact point, z_c, $q(x) = 0$ is the applied load along the beam length, E is the beam elastic modulus, I is the beam moment of inertia, and $w(x)$ is the beam deflection in the S direction. Integrating Eq. (4) results in the beam deflection equation:

$$EIw = -\frac{q}{24}x^4 + \frac{c_1}{6}x^3 + \frac{c_2}{2}x^2 + c_3 x + c_4 \tag{5}$$

where c_i are the constants of integration. The boundary conditions for the free cantilever are: clamped at the contact point, so at $x = 0$, the beam has zero displacement and slope: $w(0) = 0$ and $\frac{\mathrm{d}w(0)}{\mathrm{d}x} = 0$ (the displacement and slope of the surface are not considered in this component of the displacement). The boundary conditions at the beam tip are an applied point force, F, and zero applied moment: $\frac{\mathrm{d}^3 w(L_{\text{Free}})}{\mathrm{d}x^3} = -F/EI$ and $\frac{\mathrm{d}^2 w(L_{\text{Free}})}{\mathrm{d}z^2} = 0$. Substituting these boundary conditions into Eq. (5) results in the following values for the constants of integration:

$$c_1 = -F; \quad c_2 = FL_{\text{Free}}; \quad c_3 = c_4 = 0 \tag{6}$$

Therefore, the resulting tip deflection component due to the free beam bending is:

$$\delta_1 = \frac{FL_{\text{Free}}^3}{3EI} \tag{7}$$

For the cantilever/surface spring, the free cantilever length is given by

$$L_{\text{Free}} = L_{\text{Cant}} - l(S(z_c)) \tag{8}$$

where z_c is the contact point of the cantilever with the surface, S is the spatial function of the surface curve, and l is the arc length of the surface from $z = 0$ to $z = z_c$. In Section 2.1, we describe in detail the determination of the contact point, z_c, and arc length of the beam in contact with the surface, $l(S(z_c))$.

The second component of the cantilever tip deflection, δ_2, is due to the cantilever slope at the contact point. Because the cantilever is tangent to the surface while they are in contact, the cantilever slope equals the surface slope at the contact point. This angle at the contact point causes the added deflection, δ_2, at the cantilever tip:

$$\delta_2 = \left.\frac{\mathrm{d}S}{\mathrm{d}z}\right|_{z=z_c} \cdot L_{\mathrm{Free}} \tag{9}$$

The third component of the cantilever tip deflection, δ_3, is due to the deflection at the contact point, which equals the gap between the undeflected cantilever and surface at the contact point coordinate, z_c:

$$\delta_3 = S(z_c) \tag{10}$$

Combining δ_1, δ_2, and δ_3, the tip deflection due to force F is:

$$y = \frac{FL_{\mathrm{Free}}^3}{3EI} + \left.\frac{\mathrm{d}S}{\mathrm{d}z}\right|_{z=z_c} \cdot L_{\mathrm{Free}} + S(z_c) \tag{11}$$

Alternatively, the total deflection, y, for a known force F, and contact point z_c, can be determined by solving the beam deflection equation, Eq. (5), for the boundary conditions $w(x=0) = S(z_c)$, $\frac{\mathrm{d}w(0)}{\mathrm{d}x} = \frac{\mathrm{d}S}{\mathrm{d}z}\,|_{z=z_c}$, $\frac{\mathrm{d}^2w(x=L_{\mathrm{Free}})}{\mathrm{d}x^2} = 0$, and $\frac{\mathrm{d}w^3(x=L_{\mathrm{Free}})}{\mathrm{d}x^3} = -F/EI$. For these boundary conditions, the integration constants affected by the tip boundaries, c_1 and c_2 remain equal to those given in Eq. (6). The constants affected by the root boundaries become $c_3 = \frac{\mathrm{d}S}{\mathrm{d}z}\,|_{z=z_c}$ and $c_4 = S(z_c)$.

2.1. Determination of the contact point

The location of the contact point, z_c, along the surface is the point at which the cantilever curvature equals the surface curvature (surface contact condition):

$$\left.\frac{\mathrm{d}^2S}{\mathrm{d}z^2}\right|_{z=z_c} = \left.\frac{\mathrm{d}^2w}{\mathrm{d}z^2}\right|_{z=z_c} \tag{12}$$

where z is the axial coordinate along the surface.

This is the case because the free cantilever curvature decreases along its length (cantilever gets flatter), while the surface curvature is constant ($n = 2$) or increases ($n > 2$) along its length (surface gets rounder). z_c is the point where the surface would no longer prevent the natural curvature of the free cantilever. Alternatively, at z_c, the curvature at the root of a free cantilever of length L_{Free} subject to tip force F equals the surface curvature to which it is tangent. The boundary condition defined by Eq. (12) (beam curvature continuity) is required for static equilibrium because no external moment is applied to the beam at the contact point.

The curvature at the root of a free cantilever is:

$$\left.\frac{\mathrm{d}^2w}{\mathrm{d}z^2}\right|_{z=z_c} = \left.\frac{\mathrm{d}^2w}{\mathrm{d}x^2}\right|_{x=0} = \frac{F}{EI}L_{\mathrm{Free}} \tag{13}$$

where L_{Free} is the free cantilever length. Substituting Eq.s (2) and (13) into Eq. (12):

$$n(n-1)\frac{D}{L_{\text{Surf}}^2}\left(\frac{z_c}{\mathrm{L_{Surf}}}\right)^{n-2} = \frac{F}{EI}L_{\text{Free}} \tag{14}$$

The free cantilever length is defined as: $L_{\text{Free}} = L_{\text{Cant}} - l(S(z_c))$, where L_{Cant} is the entire cantilever length and $l(S(z_c))$ is the arc length of the cantilever segment in contact with the surface. This assumes that the cantilever segment in contact with the surface follows the surface curve exactly and does not detach from the surface. This assumption is valid because the effect of any slight lift-off on the tip displacement for a given force is negligible: any lift-off of this cantilever segment from the surface would slightly decrease the free cantilever length (decreasing δ_1 in Eq. (7)) and increase the cantilever slope at the contact point (increasing δ_2 in Eq. (9)). For long cantilevers and surfaces with small slopes, these effects are negligible compared to the total free cantilever length (during small deflections) and the displacement at the contact point, δ_3 (during large deflections).

Therefore, we set the length of cantilever in contact with the surface equal to the arc length of the surface. The arc length of the surface from $z = 0$ to z_c is:

$$l(S(z_c)) = \int_0^{z_c} \sqrt{1 + \left(\frac{\mathrm{d}S}{\mathrm{d}z}\right)^2}\,\mathrm{d}z. \tag{15}$$

For small deflections, one can assume that $(\mathrm{d}S/\mathrm{d}z)^2 \ll 1$. Then, $l(S(z_c)) = z_c$ and $L_{\text{Free}} = L_{\text{Cant}} - z_c$. In this context, the contact point equation, Eq. (14) takes the form

$$n(n-1)\frac{D}{L_{\text{Surf}}^2}\left(\frac{z_c}{L_{\text{Surf}}}\right)^{n-2} = \frac{F}{EI}\left(L_{\text{Cant}} - z_c\right) \tag{16}$$

Alternatively, one can determine the required force, F, for a given contact point, z_c, by solving eq. (14) for F:

$$F = \frac{EID}{L_{\text{Surf}}^n}n(n-1)\frac{z_c^{n-2}}{L - z_c} \tag{17}$$

where we set $L_{\text{Free}} = L - z_c$. Eq. (17) shows that the force value, F, corresponding to a given contact point, z_c, is proportional to $z_c^{n-2}/(L - z_c)$. For the contact point to increase as F increases, we require $z_c^{n-2}/(L - z_c)$ to increase as z_c increases, which can only occur if z_c^{n-2} is constant or increasing with z_c. Therefore, we require $n \geq 2$ for the spring to behave nonlinearly.

For $n = 2$, Timoshenko's original design is recovered in eq.s (14) and (17)(see Section 2.2) while for larger values of n, the contact point has a different behavior.

2.2. Force versus deflection for quadratic and general surfaces

If the spring uses Timoshenko's quadratic surface ($n = 2$) with the spatial equation given by Eq. (1), the deflections are small, and $L = L_{\text{Cant}} = L_{\text{Surf}}$, then Eq. (16) can be explicitly solved for the contact point, z_c:

$$z_c = L - \frac{2DEI}{L^2F} = L - \frac{EI}{RF} \tag{18}$$

where the constant radius of curvature $R = L^2/2D$ and the variables are defined as in Eq. (1). Then, Eq.s (3)-(12) can be combined to find the tip deflection, y, as a function of the applied tip force, F:

$$y = \begin{cases} \frac{2}{3\sqrt{3}\alpha\beta}F & \text{if } 0 \leq F \leq \sqrt{3}\alpha \\ \frac{1}{\beta} - \frac{\alpha^2}{\beta F^2} & \text{if } F > \sqrt{3}\alpha \end{cases} \tag{19}$$

where $\alpha = EI/\sqrt{3}RL$ and $\beta = 2R/L^2 = 1/D$. The nonlinearity threshold force $F_{\text{Crit}} = \sqrt{3}\alpha$ is determined by solving Eq.(13) when $L_{\text{Free}} = L$ since the cantilever will first begin to wrap around the surface at their root. Solving Eq. (13) with $L_{\text{Free}} = L$ shows that $F_{\text{Crit}} = EI/LR = \sqrt{3}\alpha$. Before contact ($F < F_{\text{Crit}}$ and $y < 2D/3$), the spring deflects in the same way as a linear cantilever beam. Eq. (19) also shows that $y \to \frac{1}{\beta} = D$ as $F \to \infty$, which agrees with what is expected to physically happen: a cantilever tip that does not overhand the surface cannot deflect beyond the surface.

For $n \geq 3$ the cantilever begins to wrap around the surface for any small, non-zero force, a property that causes essentially nonlinear spring behavior. Fig. 2 shows the contact point variation as a function of the load force for various orders of surface nonlinearity, n, when $L = L_{\text{Surf}} = L_{\text{Cant}}$, and Fig. 3 shows the contact point as a function of the cantilever tip deflection.

Fig. 4a shows the force-displacement curve for various n values. In all cases, the force reaches unbounded values as the cantilever tip approaches the critical deflection value, D. The surface nonlinearity, n, defines the smoothness of the transition to very large force values. Specifically, for small values of n, the spring force suddenly grows very large close to the critical value of deflection, D. For larger values of n, there is a smooth transition to the large-force regime that is also associated with negligible linear stiffness for very weak forces.

Fig. 4b shows the force versus deflection with a logarithmic force scale. For a typical essentially nonlinear spring with polynomial nonlinearity, the slope of the log of the reaction force is constant. In the proposed design, the slope of the log of the reaction force increases, signifying that the order of the nonlinearity increases continuously with increasing deflection. This feature of variable order of nonlinearity is inherently connected with the very large sudden increase of the reaction force for finite-displacement. It allows the proposed nonlinear element to behave as an essentially nonlinear spring for moderate excitation forces and as a vibro-impact element for very large excitation forces. The physical reason for this large sudden increase in the force is that at large enough forces, the cantilever fully wraps around the surface, and the tip cannot deflect any further.

The spring stiffness at a given force is closely related to the contact point between the cantilever and surface at that force. One can think of the spring stiffness as the stiffness of the free cantilever length. Regardless of the surface nonlinearity, n, all cantilevers have the stiffness of a full-length free cantilever when $F = y = z_c = 0$ because the surface does not yet affect the cantilever. When both the cantilever and surface have lengths, L, all springs approach infinite stiffness for large forces ($F \longrightarrow \infty$ when $y/D \longrightarrow 1$

and $z_c/L \longrightarrow 1$) because the cantilever fully wraps around the surface and the free cantilever length is zero.

For moderate force values, the free cantilever length shortens at varying rates for different n. As shown in Fig. 3, when $L = L_{\text{Surf}} = L_{\text{Cant}}$, all of the springs have contact points $z_c/L = 0$ when deflection $y/D = 0$, and $z_c/L = 1$ when deflection $y/D = 1$. Fig. 3 also shows that for larger n, the value of the contact point in between zero deflection ($y/D = 0$) and maximum deflection ($y/D = 1$) is larger than that of a smaller n surface at the same y/D value. For the z_c/L versus y/D curves to have these three qualities, the slope of the curve for a larger-n-surface must be larger for small y/D values and smaller for large y/D values. This agrees with what we expect to happen physically: the interference of the surface with the cantilever's deflection depends on the surface curvature. As n increases, the shape of the surface (with all other parameters equal) is flatter near the root and rounder near the tip. Where the surface is flatter (larger n or near the root), the contact point increases more for a given increase in tip deflection. Where the surface is rounder (smaller n or near the tip), the contact point increases less for the same increase in tip deflection.

For larger n surfaces, the rate of change in the contact point, z_c/L, for increasing deflection, y/D, for small y/D is larger than that of a smaller n surface. This means that at a given small y/D value, a larger n spring has a shorter free cantilever length and is stiffer. Therefore, at a given small force, F, the larger n spring has deflected by a smaller amount. For larger n surfaces and large deflections, y/D, the opposite is true: the rate of change in the contact point, z_c, (i.e. rate of change in free cantilever length) for increasing y/D is smaller than that of a smaller n surface. This means that for increasing large forces, F, the stiffness of a larger n spring increases less than the stiffness of a smaller n spring.

In summary, springs with larger n surfaces are stiffer at small applied forces and weaker at large applied tip forces than springs with smaller n surfaces. The spring stiffness always suddenly grows toward infinity for very large forces. The rate of sudden growth is slower for larger n surfaces. The relationship of the contact point, deflection, and spring stiffness for varying n described above is in agreement with Fig.s 2-5.

Apart from dependence on the surface nonlinearity, n, the spring's force versus deflection curve also depends on several adjustable parameters: cantilever and surface length, L, cantilever rigidity, EI, and surface maximum deflection, D. As shown in Fig. 3, the relationship between contact point/surface length, z_c/L, and displacement/maximum surface gap, y/D, is independent of L, EI, and D. When a given y/D results in a specific z_c/L, the resulting free cantilever length is $L_{\text{Free}} = L(1-z_c/L)$, where is is assumed that $L = L_{\text{Cant}} = L_{\text{Surf}}$ and D is small. While the fraction L_{Free}/L remains the same for a given deflection, y/D; a cantilever with a longer dimensionalized length, L, is a weaker spring. Consequently, a longer cantilever length results in a weaker spring for all force values. Similarly, the resulting free cantilever is more rigid when EI is larger, so a spring with a larger EI is stiffer for all force values. For larger maximum surface gaps, D, a cantilever can deflect to a larger value, y before the surface interferes with its deflection. Therefore, a spring with a larger maximum surface gap, D, is weaker.

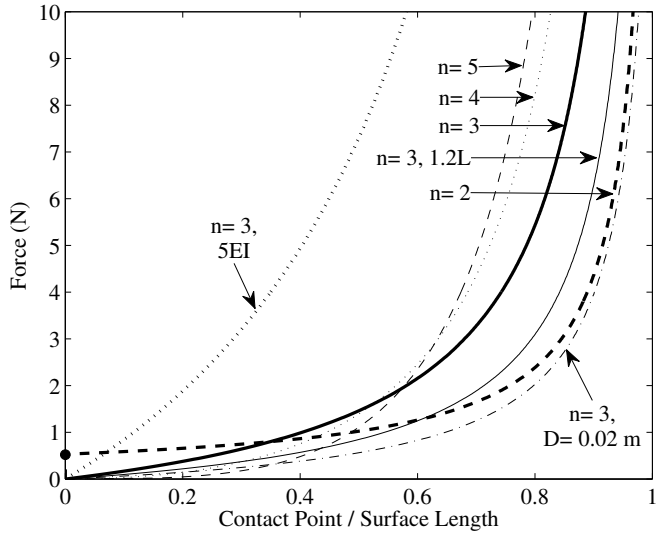

Figure 2: Theoretical tip force versus contact point (normalized by surface length) for varied spring parameters. Spring parameters are: cantilever height $h = 0.81$ mm, cantilever base $b = 4.8$ mm, elastic modulus $E = 160.6$ MPa, maximum surface gap $D = 3$ cm, and cantilever and surface lengths $L = 15$ cm. The surface curvature is varied by changing the value of n in the surface spatial function $S = D(z/L)^n$. The circle in the $n = 2$ curve is when contact between the cantilever and surface begins.

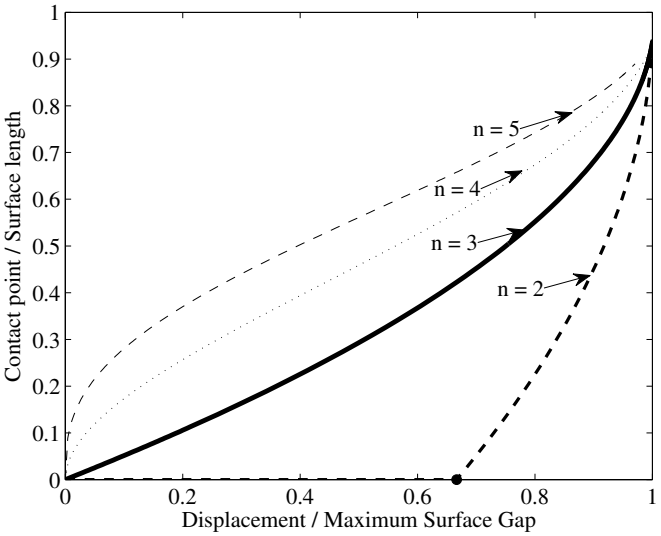

Figure 3: Theoretical contact point (normalized by surface length) versus tip displacement (normalized by maximum surface gap, D) for varied spring parameters. Each curve starts at $(0, 0)$ and ends at $(1, 1)$. The surface curvature is varied by changing the value of n in the surface spatial function $S = D(z/L)^n$. The circle on the $n = 2$ curve indicates when contact between the cantilever and surface begins. These curves are independent of the cantilever length, cross-section and elastic modulus, and the surface length and maximum surface gap, D. These curves assume that the maximum surface gap is small (they do not account for arc length) and $L_{\mathrm{Surf}} = L_{\mathrm{Cant}}$.

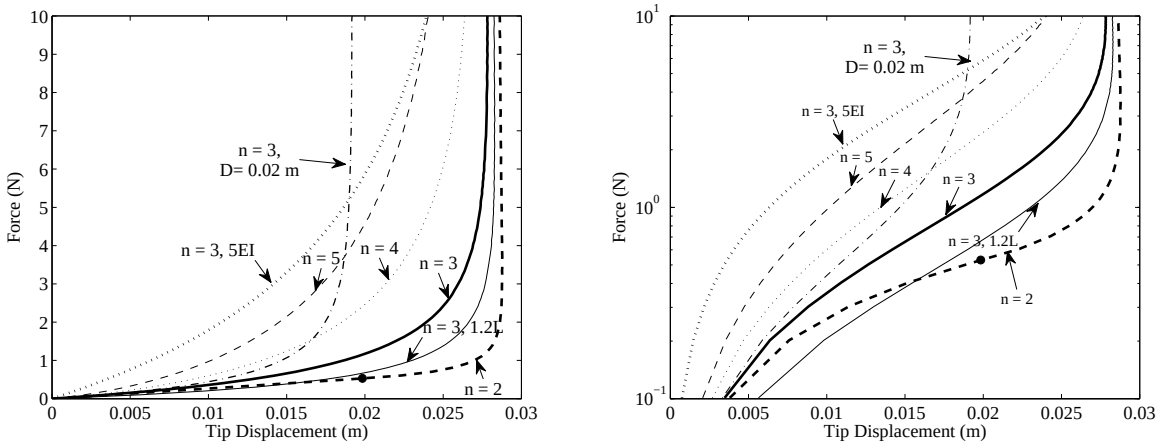

Figure 4: Theoretical force versus displacement curves for a spring with the parameters used in Fig. 2. The surface curvature is varied by changing the value of n in the surface spatial function $S = D(z/L)^n$. The circle on the $n = 2$ curve is when contact between the cantilever and surface begins. (a) Force versus displacement, linear scaling. (b) Force versus displacement, log scaling.

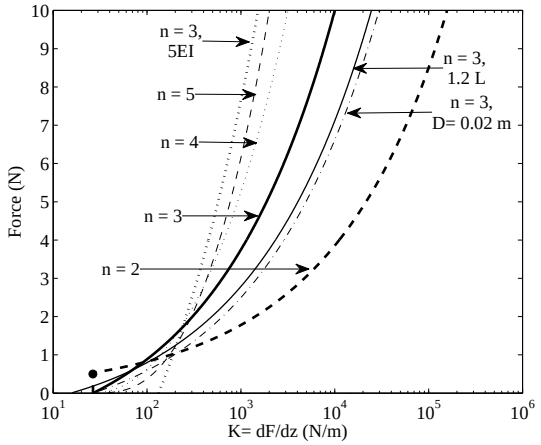

Figure 5: Theoretical tip force versus spring stiffness for varied spring parameters. Spring parameters are given in Fig. 2. n characterizes the contact surface nonlinearity. The circle on the $n = 2$ curve is when contact between the cantilever and surface begins.

2.3. Safety factor against yield

For the spring to have a long life, it needs a sufficient safety factor against yield, $SF = \sigma_{\text{Max}}/\sigma_{\text{Yield}}$, where σ_{Max} is the maximum stress in the cantilever and σ_{Yield} is the cantilever material's yield stress. For example, following common practice, we choose a safety factor against yield of 2 to give the oscillator a near-infinite fatigue life. That is, for a cantilever made out of 1095 spring steel with a yield stress of 2.3 GPa, we design the stress in the cantilever to remain below 1.2 GPa. Designing the cantilever to have a lower safety factor against yield (larger maximum stress) may shorten the device lifetime, as described in the stress versus life curves in [28].

The stress in a cantilever in pure bending is:

$$\sigma = -Ec\frac{\mathrm{d}^2 y}{\mathrm{d}z^2}. \tag{20}$$

where c is the maximum cross-section height above the cantilever's neutral axis. That is, stress in the cantilever is proportional to its curvature. As described in Section 2.1, for a given applied tip force, the maximum cantilever curvature occurs at the contact point, and at this point, the cantilever curvature, $\frac{\mathrm{d}^2 w}{\mathrm{d}z^2}$, equals the surface curvature, $\frac{\mathrm{d}^2 S}{\mathrm{d}z^2}$. The surface curvature, $\frac{\mathrm{d}^2 S}{\mathrm{d}z^2}$, increases along the surface length. Also described in Section 2.1, the value of the contact point, z_c, increases with larger applied tip forces. Therefore, when larger forces are applied, the maximum curvature (and normal stress) in the cantilever is larger and occurs at larger z values. This relationship between the contact point location, stress, and applied tip force is illustrated in Fig. 6.

The largest stress in the cantilever occurs when the contact point is at the surface end, $z_c = L_{\text{Surf}}$; that is, when the cantilever tip is deflected to the maximum value, D (assuming that the fully-deflected cantilever does not overhang the surface).

Since the largest stress in the cantilever for any applied force is proportional to the maximum surface curvature, one can design the spring to meet a safety factor against yield by setting the maximum surface curvature, $\left.\frac{\mathrm{d}^2 S}{\mathrm{d}z^2}\right|_{z=L_{\text{Surf}}}$ below a certain value.

2.4. Implementation and experimental verification

We verified the theory by performing a static force versus displacement test and a dynamic initial displacement test. We performed these tests on the nonlinear spring shown in Fig. 7. The curved surfaces of the nonlinear spring were cut on an Omax 2626 abrasive waterjet machine with a Title-A-Jet head. We used bolts to tightly clamp the cantilever between the two surfaces to minimize frictional slip, as shown in Fig. 7.

2.4.1. Force versus displacement

We measured the force versus deflection by using an Admet force tester in tension mode with a 10 N load cell as shown in Fig. 8. The cantilever/surface spring was clamped to the table, and the Admet applied the

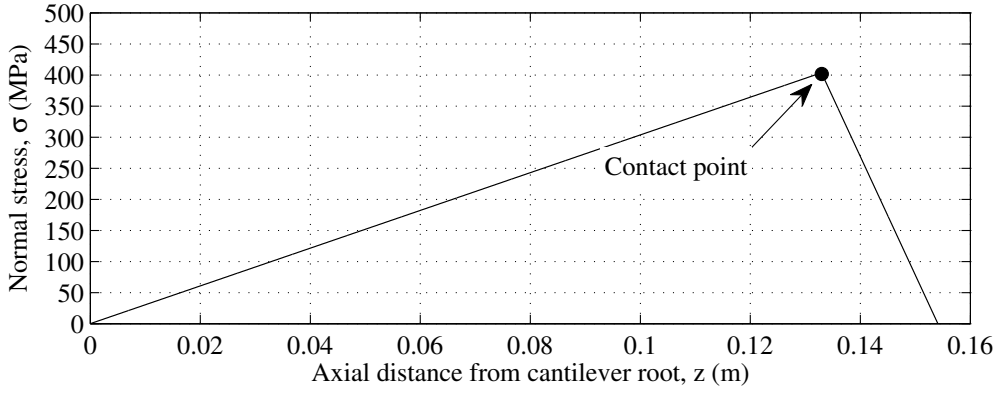

(a)

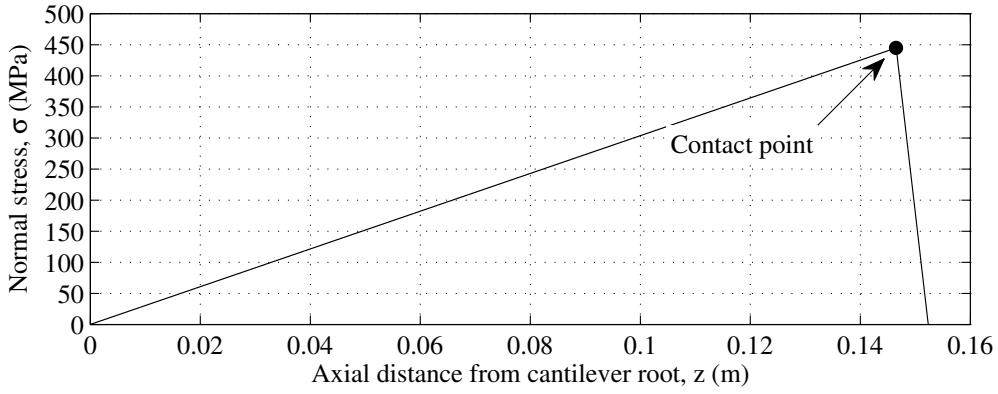

(b)

Figure 6: Simulated normal stress along the cantilever for different applied forces. The spring has the parameters used in Fig. 2. The peak in each stress curve occurs at the contact point. (a) Normal stress along cantilever when applied force, $F = 10N$. (b) Normal stress along cantilever when applied force, $F = 40N$

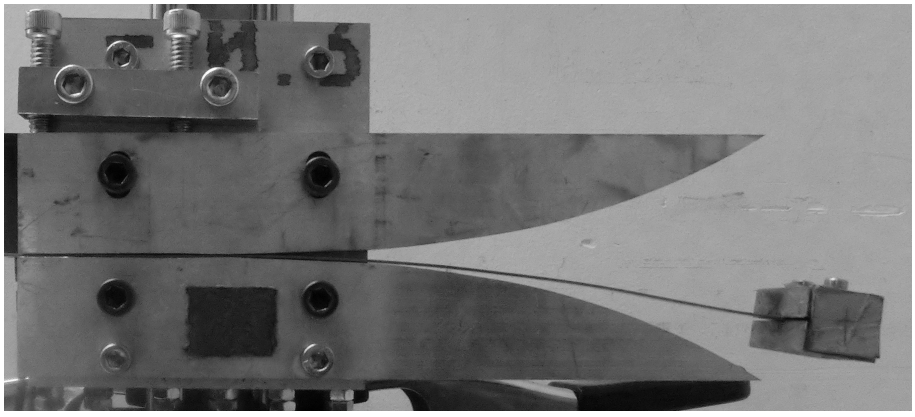

Figure 7: Implementation of the nonlinear spring. This spring has parameters: $mass$ = 60 g, L_{Cant} = 15.7 cm, spring steel elastic modulus E = 160.6 MPa, cantilever base dimension b = 4.8 mm, cantilever height h = 0.81 mm, surface length L_{Surf} = 15 cm, surface gap at surface end D = 3 cm, and surface curve power n = 3. The damping envelope of the dynamic test indicated that the viscous damping in the system is 0.007 Ns/m.

force via a 10 cm-long stiff string with two loops at its ends. One string end looped around a nut adhered to the cantilever tip. The other looped around a hook bolted to the load cell. We chose this configuration over a traditional rigid force probe so that we applied and measured only a vertical force at the cantilever tip.

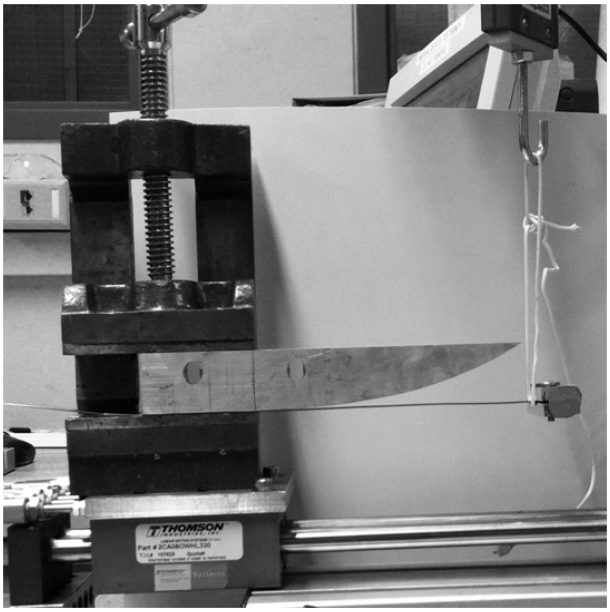

Figure 8: Force versus displacement test set-up. The Admet force tester moves the hook upwards, which pulls the string upwards, at a rate of 0.1 mm/s. The sliding Thomson rail allows us to slide the cantilever/surface spring forward as the cantilever tip is raised, in order to ensure that the string remains vertical, so that the Admet load cell measures only vertical forces.

Fig. 9 shows the test results. These results verify the theory and are repeatable. The largest error between the experiment and theory occurs for mid-range applied forces. The largest discrepancy between the experiment and theory occurs at force-value $F = 1.7$ N, when the measured displacement exceeds the theoretical displacement by 4.5%. This error may be caused by the cantilever slightly lifting off of the surface in between the cantilever root and the contact point (which causes the cantilever curvature at the contact point to be less than the theoretically predicted curvature. Therefore, less force is required for a given displacement). These experimental results highlight the singular property of this nonlinear spring: there is a maximum tip displacement for which the force theoretically approaches infinity.

2.4.2. Initial displacement test

For this test, we attached a mass to the nonlinear spring and released it from an initial displacement at $t = 0$ seconds. This experiment also used the spring shown in Fig. 7, which has the nonlinear stiffness shown in Fig. 9. The initial displacement at $t = 0$ seconds was 3.4 cm. A Samsung TL30 camera recorded the mass motion at 480 frames per second, and we used Matlab to track the position of the mass (which was colored

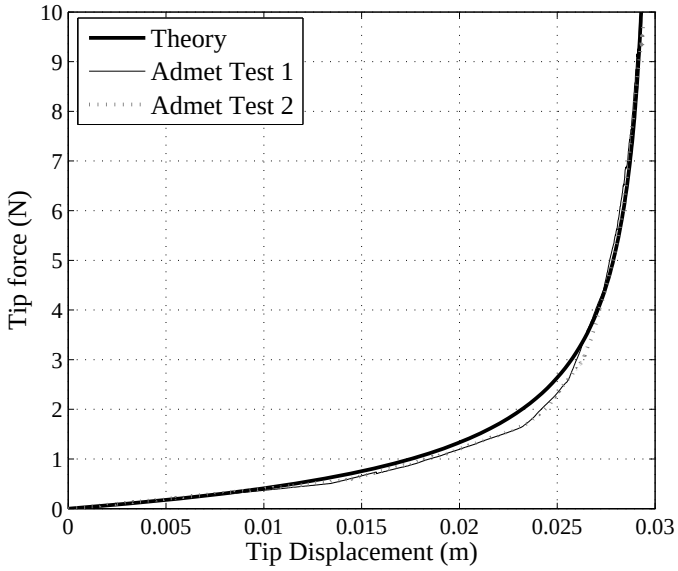

Figure 9: Force versus displacement for a cantilever/surface spring with parameters used in Fig. 7.

red). We determined the damping coefficient by using Matlab CFTOOL to curve-fit the oscillation amplitude envelope. Fig.s 10 and 11 show comparisons of the experimental time series and wavelet transforms to the theoretical predictions. The qualitative trends in the experimental dynamics over time agree well with the theory. The simulation assumes that the cantilever oscillates in its first mode only, so the higher mode frequencies shown in Fig. 11 reflect the nonlinear effect of the surfaces, rather than the free cantilever's higher vibration modes. The experimental frequencies are slightly lower than the theoretical frequencies. This might be a result of the experimental stiffness being slightly lower than the theoretical stiffness for mid-range displacements (see comments in Section 2.4.1).

The simulation models a point mass that equals the end-mass of the experimental oscillator, 60 g; with linear damping equal to the experimentally-determined damping, 0.007 Ns/m. The simulation uses the nonlinear spring stiffness predicted in Section 2, with a modification to calculate the deflection at the center of the end-mass instead of the cantilever tip. For a given force, we calculated the end-mass deflection by multiplying half the mass length by the cantilever tip slope.

The cantilever tip slope equals the slope of the free cantilever due to bending in addition to the surface slope at the contact point:

$$\frac{\mathrm{d}y}{\mathrm{d}z} = \frac{FL_{\mathrm{Free}}^2}{2EI} + \left.\frac{\mathrm{d}S}{\mathrm{d}z}\right|_{z=z_c} \cdot L_{\mathrm{Free}} \tag{21}$$

Then, the mass deflection is defined as:

$$y_{\mathrm{Mass}} = y + \frac{\mathrm{d}y}{\mathrm{d}z}\frac{L_{\mathrm{Mass}}}{2}, \tag{22}$$

where y is the cantilever tip deflection and L_{Mass} is the length of the mass in the axial direction, as labeled in Fig. 1.

Fig. 11 includes the constant frequency of a linear oscillator with the same mass and initial energy as the nonlinear spring in the initial displacement experiment.

We found the initial energy in the nonlinear spring by integrating the product of the incremental spring force and tip deflection. That is, the energy in the spring is defined as:

$$E = \int_0^{y_{\text{Mass}}} F(Y)\,\mathrm{d}Y \tag{23}$$

where y_{Mass} is the final mass displacement.

Using Eq. (11), (12), and (21)-(23) for the nonlinear spring shown in Fig. 7 with an end-mass displacement of 3.4 cm, the initial energy in the tested spring was 0.033 J. A linear oscillator with this same displacement and initial energy has a stiffness of $K = 57N/m$. If this linear oscillator had the same mass as the nonlinear oscillator (60 g), then the linear oscillator's natural frequency is 4.9 Hz. Fig. 11 shows that the nonlinear spring oscillates with multiple frequencies that exceed that of the linear spring's constant 4.9 Hz.

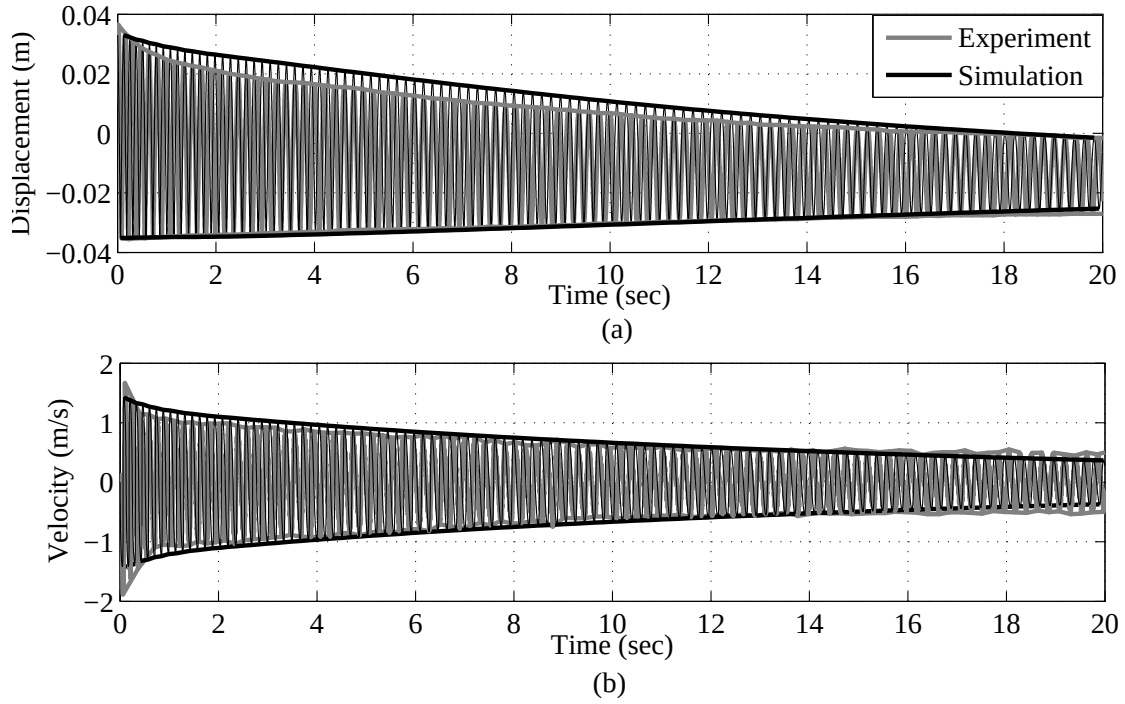

Figure 10: Time series from the initial displacement test for the nonlinear oscillator in Fig. 7. The damping envelope indicated that the viscous damping in the system is 0.007 Ns/m. (a) displacement versus time. (b) velocity versus time.

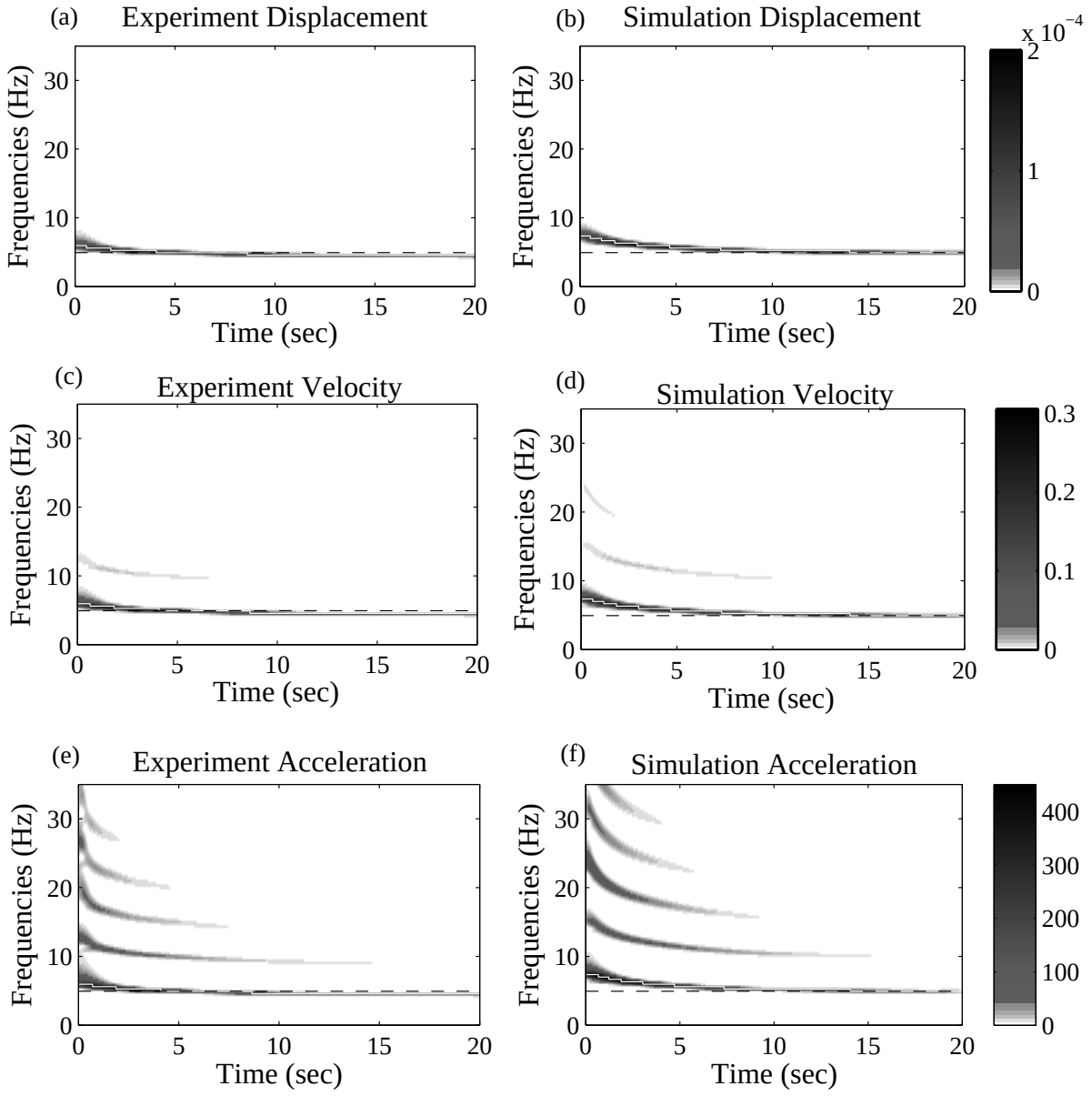

Figure 11: Wavelet transforms for the initial displacement test for the nonlinear oscillator shown in Fig. 7. Left: experiment results (a, c, e). Right: simulation results (b, d, f). The white line represents the average frequency. The black dashed line at $f = 4.9Hz$ represents the frequency of a linear mass-spring system for which the mass, initial energy, and initial displacement equal that of the tested nonlinear cantilever/surface spring system. The experimental damping envelope indicated that the viscous damping in the system is 0.007 Ns/m.

3. Energy harvesting performance and robustness from walking vibrations

Here, we numerically examine the performance of four different classes of electromagnetic energy harvesters under an excitation scenario involving walking vibrations. In particular we consider 2 linear systems, a 1DOF and a 2DOF system, as well as two nonlinear systems (also a 1DOF and a 2DOF). The linear systems use only traditional linear springs, such as helical coils, while the 1DOF nonlinear system uses the nonlinear spring described in Section 2, and the 2DOF nonlinear system uses one linear spring and two of the nonlinear springs described in Section 2. Our optimization procedure involves several iterations to optimize the many parameters (electromagnetic damping, λ, and spring stiffnesses: which includes K for the linear springs, and n and EI for the nonlinear springs) that were not constrained for optimization simplification (mass values) or practical purposes (allowable mass displacement and cantilever length when a walking person is the excitation source). Fig.s 13 and 14 (which are described in more detail below) show the optimization surfaces from the final optimization iterations. In earlier iterations, we found that setting the surface nonlinearity to $n = 3$ in the nonlinear system always increased the power compared to larger n values. This is related to how a spring with a lower n-value has lower stiffness for small displacements. We limit the smallest allowable n-value to 3 to ensure that the spring is essentially nonlinear and has a cubic spring-like stiffness (as described in Section 2), which is required for a robust energy harvester [4, 13, 14, 15]. Fig.s 13a and 13 b, therefore, show the power harvested when we vary the 1DOF nonlinear system cantilever rigidity and electromagnetic damping. Fig.s 14a and 14b show the power harvested when we vary the 2DOF nonlinear system top and middle nonlinear spring stiffnesses.

Energy harvesting by means of nonlinear dynamics has been studied in numerous contexts (see e.g. [8, 29, 22, 30, 31, 32, 33, 34, 35, 36, 37]). Recently, [17, 18] illustrated analytically, numerically, and experimentally the advantages of strong nonlinear (or targeted) energy transfers in two-degrees-of-freedom (2DOF) systems subjected to repeated impulsive excitations. Here, we use numerical simulations to examine various energy harvester configurations (linear and nonlinear with one and two DOF) and demonstrate the improved performance of a 2DOF nonlinear energy harvester over the other configurations when excited by different human motions (walking, walking quickly, and running), i.e. we focus on the continuous excitation problem.

For this application, we assume for all harvester classes that the total oscillating mass is 60 g, and the total allowable peak-peak amplitude of the mass or masses with respect to the base is 6.8 cm (that is the 1DOF mass is 60 g and can travel 6.8 cm pk-pk while each mass of the 2DOF harvester is 30 g and can travel 3.4 cm pk-pk). We constrained each of the 2DOF masses to 30g to simplify the optimization procedure. Future work will include adjusting the mass ratio and studying its effect on the energy transfer between the oscillation modes. The amplitude constraint represents the harvester casing. The energy harvesters' springs are either linear (such as a helical coil) or nonlinear (utilizing the spring described in Section 2).

The base of the energy harvester is excited by an experimentally-recorded human motion acceleration, such as a person's hip while walking or running.

We choose to extract the mechanical power via electromagnetic damping because [10] and [12], among other sources, suggest that electromagnetic transduction is more efficient than other methods such as piezoelectric for large device height:excitation displacement ratios. Our future work on this study will include considering the optimal power of energy harvesters with different transducers for a specific excitation signal.

We use the Matlab differential equation solver ode113 to numerically simulate the dynamics of energy harvesters with the configurations shown in Fig. 15. The 1DOF energy harvesters have the equation of motion:

$$m\ddot{X} = -F(X) - \lambda\dot{X} - m\ddot{h} - mg, \tag{24}$$

where m is the magnet mass, X is the magnet displacement with respect to the base, F is the force exerted by the spring, λ is the electromagnetic damping coefficient, and g is the downwards acceleration due to gravity. For the linear spring, $F = kX$, where k is the spring coefficient. For the nonlinear spring, F is a function of X and is determined using the theory described in Section 2.

The 2DOF energy harvesters have the equations of motion:

$$\begin{array}{l} m_{\text{Top}}\ddot{X} = -F_{\text{Top}}(X) - F_{\text{Mid}}(X-Z) - \lambda_{\text{Top}}\dot{X} - \lambda_{\text{Mid}}(\dot{X}-\dot{Z}) - m_{\text{Top}}\ddot{h} - m_{\text{Top}}g \\ m_{\text{Bot}}\ddot{Z} = -F_{\text{Bot}}(Z) + F_{\text{Mid}}(X-Z) - \lambda_{\text{Bot}}\dot{Z} + \lambda_{\text{Mid}}(\dot{X}-\dot{Z}) - m_{\text{Bot}}\ddot{h} - m_{\text{Bot}}g \end{array} \tag{25}$$

where m_{Top} is the top magnet mass, m_{Bot} is the bottom magnet mass, X is the top magnet displacement with respect to the base, Z is the bottom magnet displacement with respect to the base, F_i are the forces of the linear or nonlinear springs connecting the masses to each other or the base, λ_i are the electromagnetic damping coefficients, and g is the downwards acceleration due to gravity, as shown in Fig. 15.

The equations of motion, Eq.s (24) and (25), consider all masses except the proof masses to be negligible. This assumption is valid because the spring steel cantilevers each weigh only a few grams while the proof masses weigh 30 or 60 grams. The simulated power harvested by each system is the power dissipated by each electromagnetic damper: $P = \lambda\dot{X}^2$ for the 1DOF system and $P = \lambda_{Top}\dot{X}^2 + \lambda_{Mid}(\dot{X}-\dot{Z})^2 + \lambda\dot{Z}^2$ for the 2DOF systems. Unless otherwise stated, the simulations assume that mechanical damping is negligible. This assumption is valid because the minimum electromagnetic damping considered is 0.05 Ns/m, while the experimentally measured mechanical damping is on the order of 0.007 Ns/m. A detailed analysis of the effects of parasitic damping is given in Section 3.2.

When the mass travels the maximum distance, y_{Crit}, it collides with the outer casing. We modeled elastic collisions in our numerical simulation by modifying the spring forces to approach infinity for mass displacements, y, near and exceeding the displacement constraints. The modified spring force is defined as:

$$F_{\text{Simulated}} = \begin{cases} F_{\text{Theoretical}}(y) + \frac{\epsilon}{y - y_{\text{Crit}}} & \text{if } y < 0.99y_{\text{Crit}} \\ F_{\text{Theoretical}}(0.99y_{\text{Crit}}) + \frac{\epsilon}{0.01y_{\text{Crit}}} + \frac{1}{\epsilon}\left(\frac{y}{y_{\text{Crit}}}\right)^{\gamma} & \text{if } y \geq 0.99y_{\text{Crit}} \end{cases} \tag{26}$$

where the sensitivity parameters ϵ and γ were set to $\epsilon = 10^{-5}$ Nm and $\gamma = 5$. Using Eq. 26, the simulated force effectively equals the theoretical force for y values significantly less than y_{Crit}. When $y \geq 0.99 y_{\text{Crit}}$, the simulated force is effectively determined by ϵ. Smaller ϵ allows the mass to travel closer to the displacement constraints before being repelled by a large force, while larger ϵ repel the mass away from the constraints sooner. If a numerical error in the simulation allows the mass to displace beyond its constraints, $y \geq y_{\text{Crit}}$, then the simulation repels the mass away from the constraints with a force proportional to $\frac{1}{\epsilon}\left(\frac{y}{y_{\text{Crit}}}\right)^{\gamma}$. Larger values of γ increase this force. The numerical simulation is insensitive to the specific values of ϵ and γ because all values serve to effectively simulate an elastic collision for one time step before normal dynamics resume.

We use the numerical simulation to optimize the four energy harvester configurations (1DOF, 2DOF; nonlinear and linear) for human motion according to the following criteria: we want to maximize the power harvested during both walking and running, with the constraint that parameters maximizing walking power are chosen if no set of parameters produces non-negligible power (> 0.01 W) for both walking and running excitations. We choose this criteria assuming that our target end-user carrying the energy harvester walks more often than runs.

The simulations excited energy harvesters at the base by the experimentally-recorded accelerations of a person's hip while walking, walking quickly, and running (Fig. 12 shows this acceleration signal as well as the associated spectrum). The signals were measured using a Vernier 25-g accelerometer with temporal resolution of 1,000 samples per second. The accelerometer was rated to measure acceleration signals with frequencies from 0-100 Hz.

Fig. 13 shows the optimization surfaces for the 1DOF systems when excited by the hip walking and running motions. The parameters that we optimized in this case were the electromagnetic damping coefficient and the cantilever rigidity (for the nonlinear system) or linear spring stiffness (for the linear system), taking into account that the damping has to include the mechanical losses (so it cannot reach values lower than the mechanical damping). For the simulations, we used time steps of 10^{-4} seconds. To calculate the harvested power we computed the energy dissipated (or harvested) after 15 seconds so that the initial transient effects had minimal influence. Fig. 13 shows that the nonlinear system has a set of parameters that harvest significant (> 0.01 W) power during both walking and running. However, the linear system does not have any overlap in the parameters that produce non-negligible power for both the walking and running excitations.

Fig. 14 shows the optimization surfaces for the 2DOF systems excited by the walking and running motions. The 2DOF systems require more effort to optimize since they involve several parameters rather than just two. To keep the optimization problem simple, we restrict our analysis to the case of equal masses. Despite this constraint we still obtain significant improvement in power by the 2DOF nonlinear system compared with the other configurations. However, the mass distribution may play an important

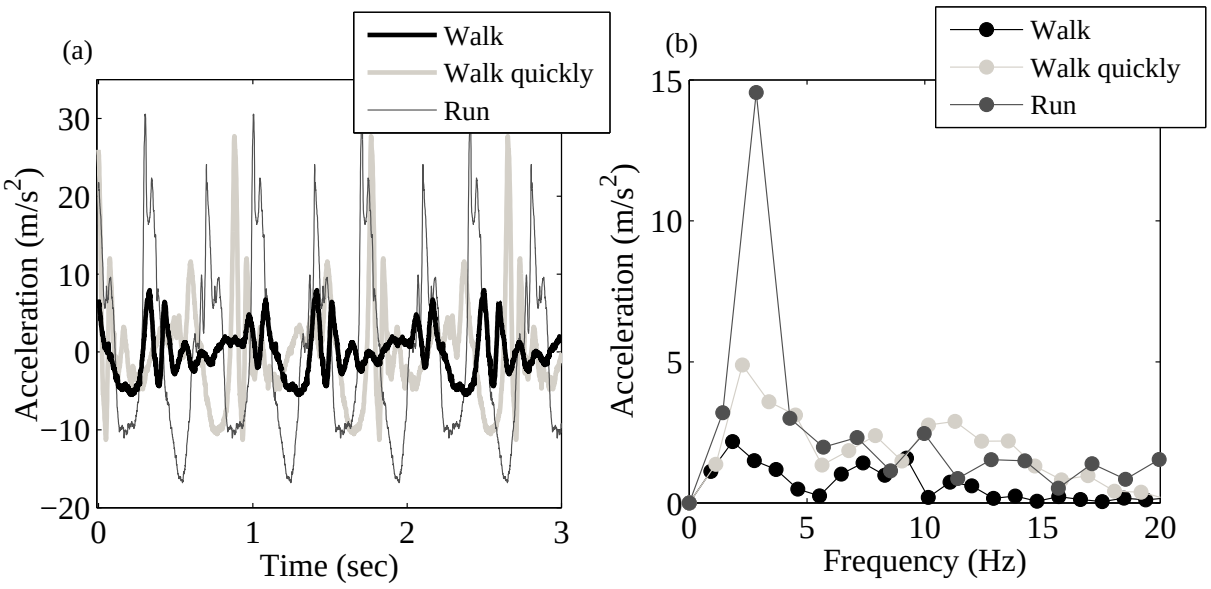

Figure 12: Experimentally recorded acceleration of a person's hip while walking and running. (a) Time series. (b) Moduli of the fast frequency transform of the time series. The presented accelerometer data as well as others can be found in [38] and [39].

role on the performance and its role should be investigated further in the future. For further simplicity, we restrict the 2DOF oscillators to have $\lambda_{Top} = \lambda_{Bot} = 0.001$ Ns/m (a theoretical idealization of negligible parasitic damping) and $\lambda_{Mid} = 1.6$ Ns/m because a large middle electromagnetic damping coefficient tends to increase the system's robustness to parasitic damping. More details on the optimization procedure can be found in [38]. Similarly to the 1DOF systems, the 2DOF nonlinear harvester has a set of parameters that generate non-negligible power (> 0.01 W) for both walking and running while the 2DOF linear harvester does not have a set of parameters that can do this.

Fig. 15 lists the chosen system parameters for each harvester. We examine the system adaptivity in Section 3.1. We examine the detailed role of the parasitic damping in Section 3.2.

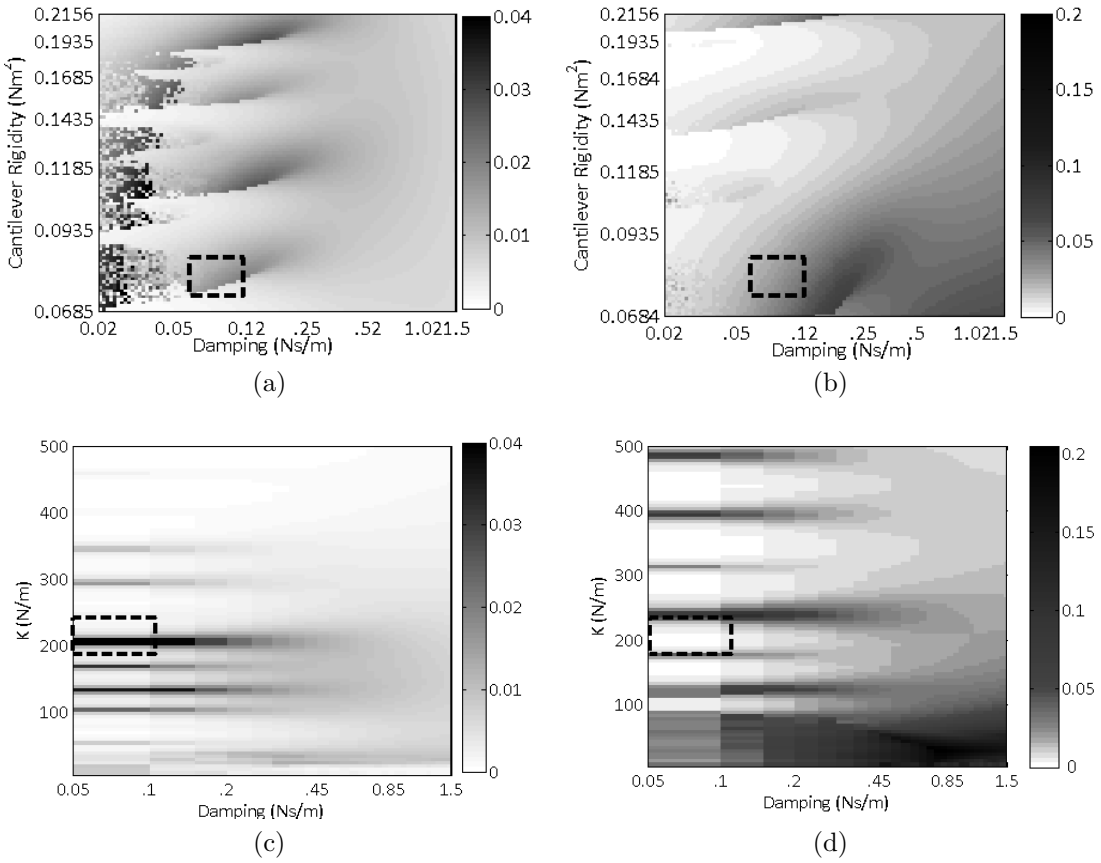

Figure 13: Power (W) Harvested by 1DOF systems with varied stiffness and electromagnetic damping coefficients. (a) Nonlinear system excited by walking, (b) Nonlinear system excited by running, (c) Linear system excited by walking, (d) Linear system excited by running. The dashed line boxes compare the power harvested by certain sets of parameters when excited by walking or running. Both systems have mass $m = 60$ g, and the peak-peak displacement of the mass relative to the surfaces is constrained to 6.8 cm. The nonlinear harvester has parameters: cantilever length $L_{\text{Cant}} = 15.7$ cm, surface length $L_{\text{Surf}} = 15$ cm, surface gap at surface end $D = 3$ cm, and surface curve power $n = 3$.

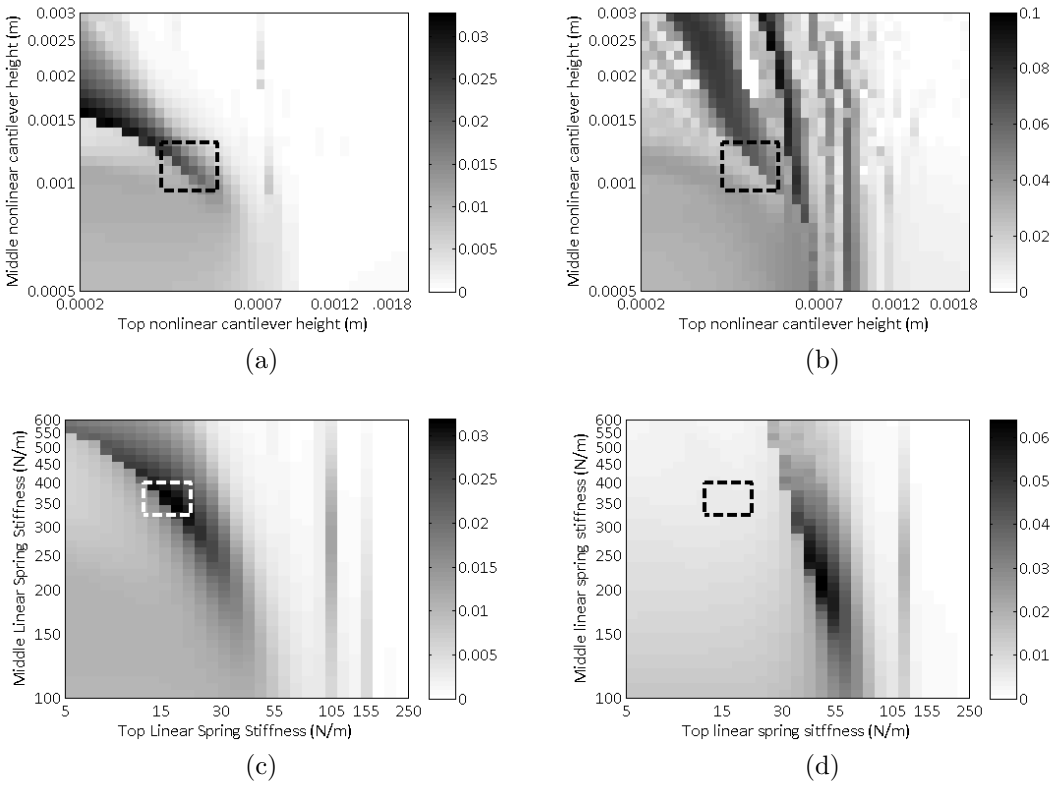

Figure 14: Power (W) Harvested by 2DOF systems with varied stiffness and electromagnetic damping coefficients. (a) Nonlinear system excited by walking, (b) Nonlinear system excited by running, (c) Linear system excited by walking, (d) Linear system excited by running. The dashed line boxes compare the power harvested by certain sets of parameters when excited by walking or running. Both systems have $m_{Top} = m_{Bot} = 30$ g, $K_{Bot} = 205$ N/m, $\lambda_{Top} = \lambda_{Bot} = 0.001$ Ns/m, and $\lambda_{Mid} = 1.6Ns/m$. The total peak-peak displacement of the masses relative to the surfaces is constrained to 6.8 cm. The nonlinear springs have parameters: cantilever length $L_{\text{Cant}} = 10$ cm, cantilever elastic modulus, $E = 160$ GPa, surface length $L_{\text{Surf}} = 10$ cm, surface gap at surface end $D = 1.5$ cm, and surface curve power $n = 3$.

(a)

1DOF Linear	
λ (Ns/m)	0.05
K (N/m)	205

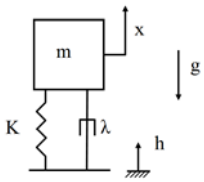

(b)

1DOF Nonlinear	
λ (Ns/m)	0.136
L_{cant} (cm)	15.7
EI (Nm^2)	8.000×10^{-4}

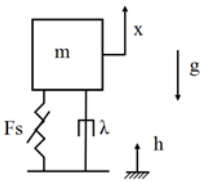

(c)

2DOF Linear	
$\lambda_{Top} = \lambda_{Bot}$ (Ns/m)	0.001
λ_{Mid} (Ns/m)	1.6
K_{Top} (N/m)	345
K_{Mid} (N/m)	17
K_{Bot} (N/m)	205

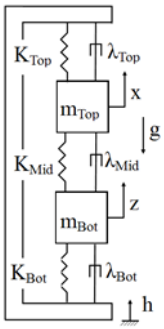

(d)

2DOF Nonlinear	
$\lambda_{Top} = \lambda_{Bot}$ (Ns/m)	0.001
λ_{Mid} (Ns/m)	1.6
EI_{Top} (N/m^2)	6.367×10^{-4}
$L_{Cant,Top}$ (cm)	10
EI_{Mid} (N/m^2)	6.374×10^{-3}
$L_{Cant,Mid}$ (cm)	10
K_{Bot} (N/m)	205

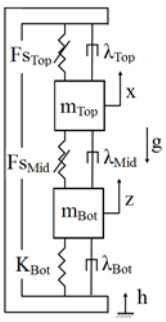

Figure 15: Summary of optimal energy harvesters. (a) 1DOF linear system, (b) 1DOF nonlinear system, (c) 2DOF linear system, (d) 2DOF nonlinear system. For the 1DOF systems, the mass is 60 g. For the 2DOF systems, each mass is 30 g. For all the nonlinear springs, the contact surface has the same length as the cantilever, and its nonlinearity is $n = 3$. For the 1DOF nonlinear system, the cantilever/surface spring's maximum surface gap, D is 3 cm (mass overhang allows the mass to travel ± 6.8 cm with respect to the surface). For the 2DOF nonlinear systems, each nonlinear cantilever/surface spring has a maximum surface gap of 1.5 cm in each direction (mass overhang allows the mass to travel ± 3.4 cm wrt the surface).

3.1. Robustness to variability of the excitation

We present the power harvested for each optimized system configuration in Fig. 16. We measure the harvesters' adaptivity by comparing the power harvested by each system when its base is excited by different human motion signals: walking, walking quickly, and running (the specific parameter optimization criteria, as described earlier in Section 3, is to maximize the harvested power for both walking and running, with the constraint that we choose the system that produces nonnegligible power [> 0.01 W] during walking if no parameter set produces nonnegligible power during both walking and running).

Fig. 16 shows that the 1DOF linear system with light damping harvests the most power when excited by the hip walking signal. The system that harvests the second largest amount of power is the 2DOF linear system. However, when we focus on the overall performance (i.e. consider different excitation scenarios), we observe that the optimal 2DOF nonlinear system presents the maximum average performance, and the linear systems adapt very poorly when the excitation signal is different than the optimized signal.

The optimized 1DOF nonlinear system power can never exceed the optimal 1DOF linear system power, in agreement with the analysis presented in [29]. Nevertheless, the 1DOF nonlinear system has better adaptivity to different excitation signals, as shown by the higher average power compared with 1DOF linear system.

To better understand this very good property of the 2DOF nonlinear system, we consider the response time series as well as the corresponding wavelet transforms. More specifically, in Fig. 17 we present the time series for the 2DOF linear and nonlinear systems under hip-walking and running motions. Fig. 18 shows the corresponding wavelet transforms, and Fig. 19 shows the instantaneous harvested power versus time. As expected, there is a single dominant frequency associated with the resonant frequency of the linear oscillator. This carefully chosen resonant frequency gives very good harvesting performance when the excitation signal is the one for which we optimized, but the performance falls very fast when we move away from this excitation form.

In contrast to the linear systems, where resonance occurs directly between the excitation and the mode that harvests energy, for the 2DOF nonlinear system the primary harvesting mechanism is not the resonance of the excitation with the harvesting mode but rather the nonlinear energy transfer mechanism which continuously moves energy to the harvesting mode. This nonlinear energy transfer mechanism (or targeted energy transfer) has been studied extensively in similar systems under impulsive excitation [4, 5] or periodic impulsive excitation [17, 18]. Fig. 16 illustrates how this mechanism is associated with strong adaptivity under continuous periodic excitations with different spectra. This good property is in full accordance with the fact that the targeted energy transfer plays the dominant role in the energy harvesting rather than resonance. The detailed analysis of the targeted energy transfer mechanism under this kind of excitation is beyond the scope of this work and will be studied extensively in the future.

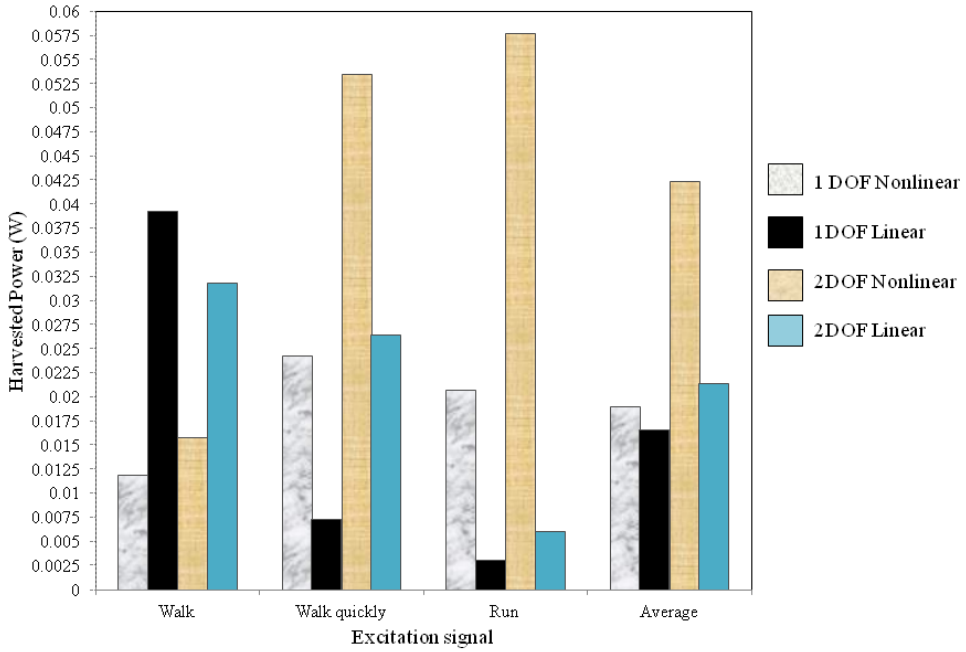

Figure 16: Simulated power harvested by energy harvesters with the configurations and optimized parameters given in Fig. 15. The parameters were optimized for maximum power during both walking and running, with the constraint that a non-negligible amount of power should be harvested during walking.

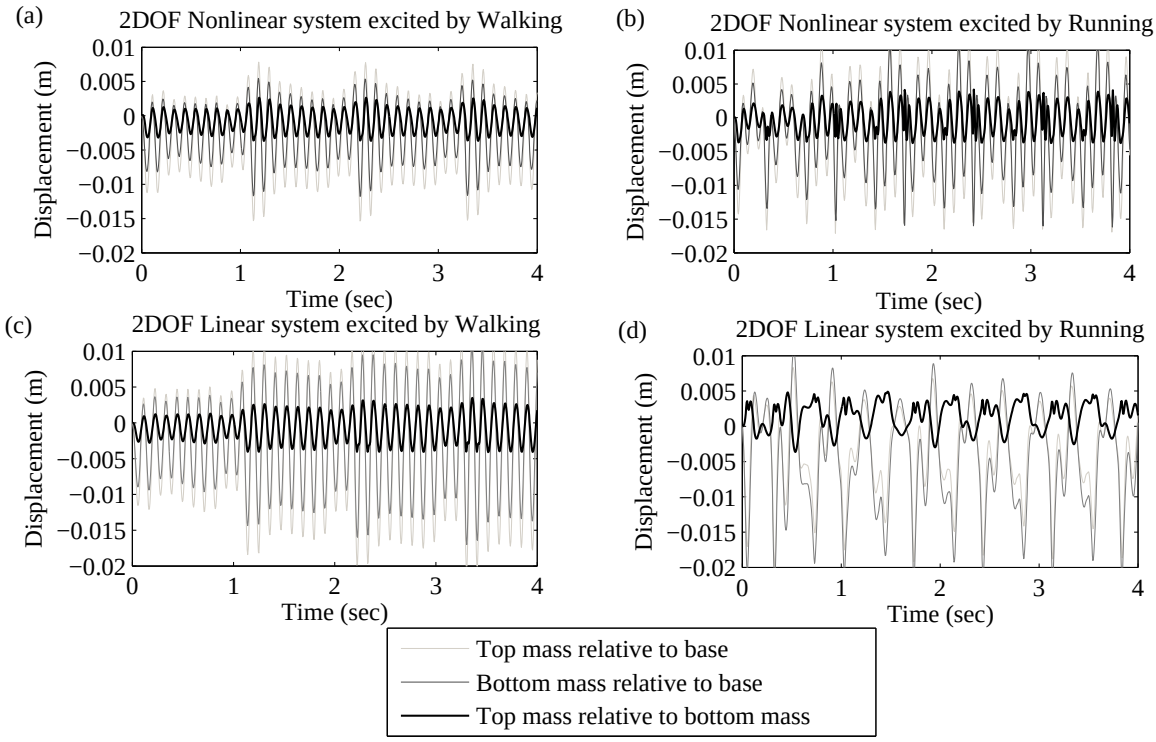

Figure 17: Displacement time series of the optimized 2DOF nonlinear and linear systems when excited at the base by the acceleration of a person's hip while walking (a, c) and running (b, d). The system parameters are listed in Fig. 15. The time series of other optimized systems can be found in [38].

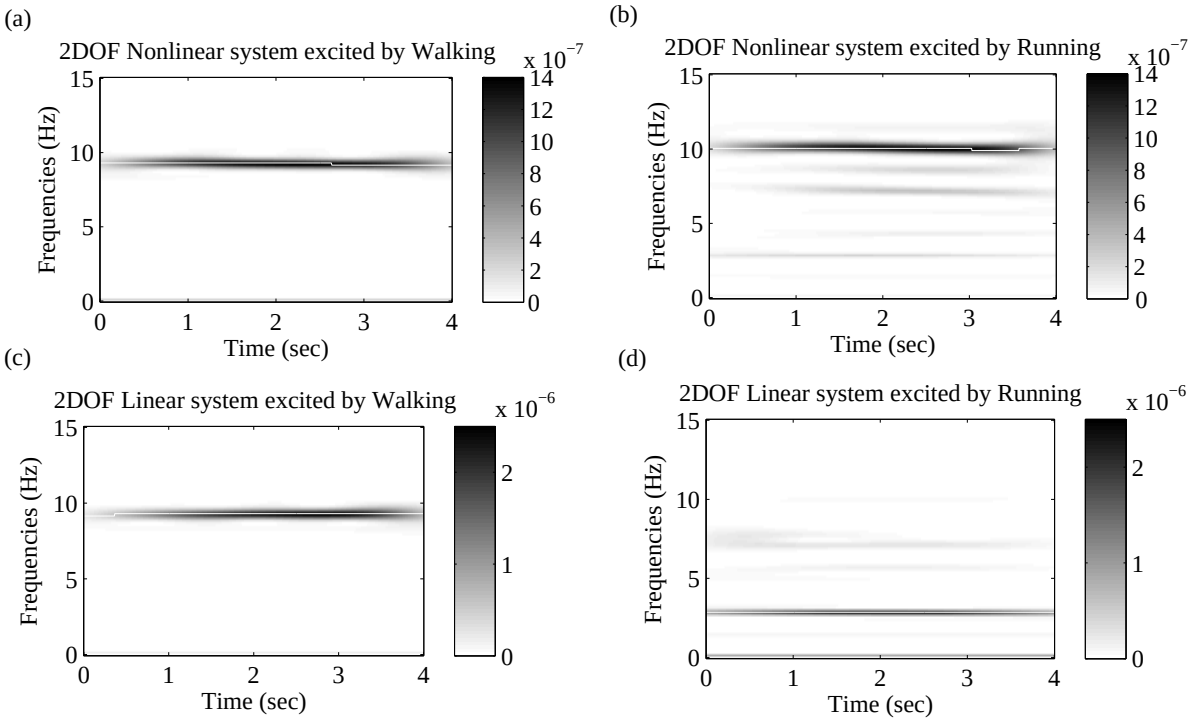

Figure 18: Wavelet transforms of the top mass displacement relative to the bottom mass displacement for the optimized 2DOF nonlinear and linear systems when excited at the base by the acceleration of a person's hip while walking (a, c) and running (b, d). The system parameters are listed in Fig. 15.

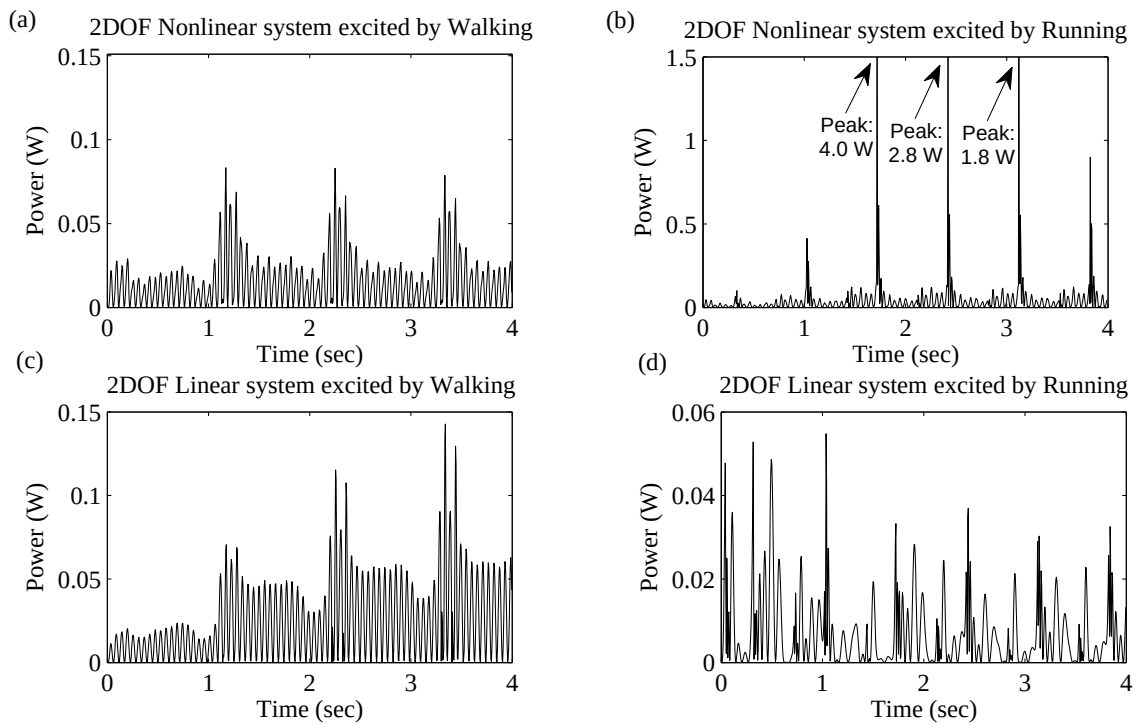

Figure 19: Instantaneous power harvested by the optimized 2DOF nonlinear and linear systems when excited at the base by the acceleration of a person's hip while walking (a, c) and running (b, d). The system parameters are listed in Fig. 15.

3.2. Robustness to parasitic damping

Here, we compare the effect of mechanical damping and electrical inefficiencies on the harvested power of the different systems. Experiments showed that the mechanical damping for the 1DOF harvester is on the order of 0.01 Ns/m [38].

To calculate the harvested power when parasitic damping is present, we account for parasitic damping in the damping coefficients determined by the optimization procedure (Fig.s 13, 14, and 15). That is, we set $\lambda = \lambda_{\text{EM}} + \lambda_{\text{Parasitic}}$, where λ is the optimal damping coefficient found in Fig.s 13 and 14, λ_{EM} is the electromagnetic damping and $\lambda_{\text{Parasitic}}$ is the undesirable parasitic damping. While the total dissipated power is $P_{\text{Dissipated}} = \lambda \dot{X}^2$ (or $P_{\text{Dissipated}} = \lambda(\dot{X} - \dot{Z})^2$), the power converted to electricity is $P_{\text{Harvested}} = \lambda_{EM} \dot{X}^2$ (or $P_{\text{Harvested}} = \lambda_{EM}(\dot{X} - \dot{Z})^2$) for the 1DOF (2DOF) systems. We chose to set the parasitic damping, $\lambda_{\text{Parasitic}}$, to 0.025 Ns/m.

Fig. 20 shows the power conversion efficiency for each system after accounting for the parasitic damping. This efficiency is independent of the excitation signal. We define the power conversion efficiency as $\eta = P_{\text{Harvested}}/(P_{\text{Harvested}} + P_{\text{Parasitic}})$: it is the fraction of theoretical power (0 Ns/m parasitic damping) that is harvested when 0.025 Ns/m parasitic damping is present. We observe that the 1DOF linear system with low electromagnetic damping harvests only 50% of its optimal power when 0.025 Ns/m parasitic damping is present. On the other hand, the other three oscillators, which have larger optimal damping coefficients, have significantly less power decay. The 1DOF nonlinear oscillator (which has an optimal damping coefficient $\lambda = 0.13$ Ns/m) still harvests 81% its optimal power, and the 2DOF oscillators (with damping $\lambda = 1.6$ Ns/m) still harvest 98% their optimized power. The 2DOF harvesters retain most of their power while the 1DOF linear harvester loses a lot of its power to added parasitic damping because 0.025 Ns/m parasitic damping is only 2% of the 2DOF nonlinear harvester's electromagnetic damping while it is 50% of the 1DOF linear harvester's electromagnetic damping. Additionally, we note that the 1DOF nonlinear harvester's optimal parameters are less sensitive to added damping than the linear system's.

Thus, the key feature for the excellent robustness of the 2DOF nonlinear system to parasitic damping is the fact that optimal energy harvesting occurs for large values of damping. This characteristic is related to how the energy transfer mechanism moves large amounts of energy in the harvesting mode without the requirement of a resonance condition.

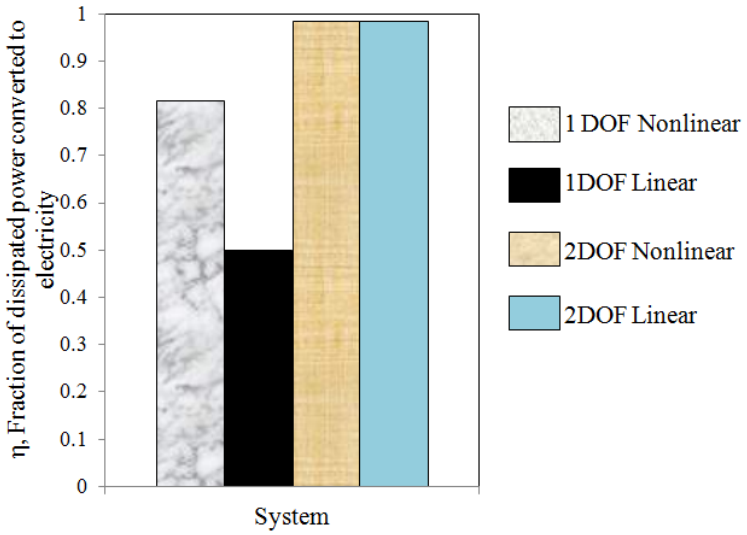

Figure 20: Power conversion efficiency: assuming fixed parasitic damping (0.06 Ns/m) for all configurations we compute the power conversion efficiency for each set of optimal performance parameters.

4. Conclusions and future work

We have illustrated how nonlinearity can be utilized to improve robustness of energy harvesting under continuous excitation with uncertain characteristics. The proposed design consists of a 2DOF nonlinear configuration. The essentially nonlinear springs utilized are designed by means of cantilever beams and contact surfaces with a carefully chosen distribution of curvature. The design has minimal frictional losses and moving parts, which increases the device lifetime. Additionally, the spring force has a nonlinear dependence on the displacement for which the order of nonlinearity increases as the displacement increases. This behavior results in theoretically infinite spring force for a critical finite displacement, which protects the spring from extreme loading conditions. Using structural mechanics arguments, we have derived analytic expressions for the response of the nonlinear element and studied its properties. The analytic expressions were verified experimentally by force versus displacement static tests and initial displacement dynamic tests with time-series and wavelet transforms.

We performed a systematic study of four types of harvesting systems involving 1DOF and 2DOF, linear and nonlinear systems. For each case, we used an experimentally measured excitation (acceleration) signal to optimize the system parameters. We then compared the performance of the optimal nonlinear and linear (1DOF and 2DOF) energy harvesters in terms of their power output, adaptivity to different human motions, and robustness to parasitic damping. We found that even though the 1DOF linear system has the best performance in terms of maximum power when designed for a given excitation signal, its harvested power is very sensitive to small changes of the excitation signal. Equally important, the 1DOF system has

very poor power conversion efficiency when the parasitic damping is taken into account. On the other hand the 1DOF nonlinear system has excellent behavior in the presence of parasitic damping. The optimized 2DOF nonlinear system maintains this property and, in addition, has the best average performance over different excitation signals. We interpreted this 2DOF nonlinear system behavior as a result of the strong nonlinear energy transfers which have been observed in the past for impulsive excitation and for which we have now demonstrated for continuous excitation with a smooth spectrum.

Future steps involve the analytic study of the 2DOF nonlinear system and the formulation of conditions for nonlinear energy transfer between modes in the presence of periodic excitation with continuous spectra. Our aim in this case will be to investigate the benefits of nonlinear energy transfers between modes on the energy harvesting performance and robustness. From an implementation point of view, the authors are currently working on fabricating a full energy harvester prototype (with the electromagnetic component) along the lines described in the presented work. With the prototype, we will perform actual walking experiments to measure the device's dynamics and generated electricity.

5. Acknowledgments

We are grateful to the Naval Engineering Education Center for support under Grant No. 3002883706 as well as to the National Science Foundation for support of JMK through the Graduate Research Fellowship Program under Grant No. 1122374. We also gratefully acknowledge support by the MIT Energy Initiative through the project 'Efficient nonlinear energy harvesting from broad-band vibrational sources by mimicking turbulent energy transfer mechanisms'. Patents have been filed based on the research results presented in this manuscript.

References

[1] T. von Büren, P. Mitcheson, T. Green, E. Yeatman, A. Holmes, G. Tröster, Optimization of inertial micropower generators for human walking motion, IEEE Sensors Journal 6 (1) (2006) 28–38.

[2] J. Paradiso, T. Starner, Energy scavenging for mobile and wireless electronics, IEEE Pervasive Computing 4 (1) (2005) 18–27.

[3] L. Manevitch, A. Musienko, C. Lamarque, New analytical approach to energy pumping problem in strongly nonhomogeneous 2dof systems, Meccanica (2007) 77–83.

[4] A. Vakakis, O. Gendelman, L. Bergman, D. McFarland, G. Kerschen, Y. S. Lee, Nonlinear Targeted Energy Transfer in Mechanical and Structural Systems, Springer, 2009.

[5] T. Sapsis, D. Quinn, A. Vakakis, L. Bergman, Effective stiffening and damping enhancement of structures with strongly nonlinear local attachments, J. Vibration and Acoustics 134 (1).

[6] Y. Lee, A. Vakakis, L. Bergman, D. McFarland, G. Kersche, Suppressing aeroelastic instability using broadband passive targeted energy transfers, part 1: Theory, AIAA Journal 45 (3) (2007) 693–711.

[7] B. Vaurigaud, L. Manevitch, C. Lamarque, Suppressing aeroelastic instability in a suspension bridge using a nonlinear absorber, in: IUTAM Symposium on Nonlinear Dynamics for Advanced Technologies and Engineering Design, Vol. 32, 2013, pp. 263–277, (closed).

[8] S. Stanton, C. McGehee, B. Mann, Nonlinear dynamics for broadband energy harvesting: Investigation of a bistable piezoelectric inertial generator, Physica D 239 (2010) 640–653.

[9] X. Tang, L. Zuo, Simulation and experiment validation of simultaneous vibration control and energy harvesting from buildings using tuned mass dampers, in: Proceedings of the American Control Conference, 2011, pp. 3134–3139.

[10] P. Mitcheson, T. Green, Y. E.M., H. A.S., Architectures for vibration-driven micropower generators, J. Microelectromechanical Systems.

[11] O. Yaglioglu, Modeling and design considerations for a micro-hydraulic piezoelectric power generator, Master's thesis, Massachusetts Institute of Technology (2002).
[12] A. Trimble, Energy harvesting of random wide-band vibrations with applications to an electro-magnetic rotational energy harvester, Ph.D. thesis, Massachusetts Institute of Technology (2011).
[13] O. Gendelman, T. Sapsis, A. Vakakis, L. Bergman, Enhanced passive targeted energy transfer in strongly nonlinear mechanical oscillators, J. of Sound and Vibration 330 (2011) 1–8.
[14] T. Sapsis, A. Vakakis, O. Gendelman, L. Bergman, G. Kerschen, D. Quinn, Efficiency of targeted energy transfers in coupled nonlinear oscillators associated with 1:1 resonance captures: Part ii, analytical study, J. Sound and Vibration (2009) 297–320.
[15] D. Quinn, O. Gendelman, G. Kerschen, T. Sapsis, L. Bergman, A. Vakakis, Efficiency of targeted energy transfers in coupled nonlinear oscillators associated with 1:1 resonance captures: Part i, J. Sound and Vibration (2008) 1228–1248.
[16] D. McFarland, L. Bergman, A. Vakakis, Experimental study of non-linear energy pumping occurring at a single fast frequency, International Journal of Non-Linear Mechanics 40 (2005) 891–899.
[17] K. Remick, A. Vakakis, L. Bergman, D. M. McFarland, D. D. Quinn, T. Sapsis, Sustained dynamical instabilities in coupled oscillators with essential nonlinearities, ASME J. Vibration and Acoustics 136 (2014) 011013.
[18] K. Remick, H.-K. Joo, D. McFarland, T. Sapsis, L. Bergman, D. Quinn, A. Vakakis, Sustained high-frequency energy harvesting through a strongly nonlinear electromechanical system under single and repeated impulsive excitations, J. Sound and Vibration.
[19] A. Hajati, S. Bathurst, H. Lee, S. Kim, Design and fabrication of a nonlinear resonator for ultra wide-bandwidth energy harvesting applications, in: Proceedings of the IEEE International Conference on Micro Electro Mechanical Systems (MEMs), 2011, pp. 1301–1304.
[20] D. Freeman, Nonlinear springs with applications to flow regulation valves and mechanisms, Ph.D. thesis, Massachusetts Institute of Technology (2008).
[21] F. Cottone, H. Vocca, L. Gammaitoni, Nonlinear energy harvesting, Physical Review Letters 102 (8).
[22] B. Mann, N. Sims, Energy harvesting from the nonlinear oscillations of magnetic levitation, J. Sound and Vibration 319 (2009) 515–530.
[23] A. Carrella, M. Brennan, T. Waters, K. Shin, On the design of a high-staticlow-dynamic stiffness isolator using linear mechanical springs and magnets, J. Sound and Vibration 315 (2008) 712–720.
[24] I. Kovacic, M. Brennan, T. Waters, A study of a nonlinear vibration isolator with a quasi-zero stiffness characteristic, J. Sound and Vibration 315 (2008) 700–711.
[25] S. Timoshenko, Strength of Materials, Van Nostrand, 1955.
[26] J. Li, Electrostatic zipping actuators and their application to mems, Ph.D. thesis, Massachusetts Institute of Technology (2004).
[27] J. Li, M. Brenner, T. Christen, M. Kotilainen, J. Lang, A. Slocum, Deep reactive ion-etched compliant starting zone electrostatic zipping actuators, J. Microelectromechanical Systems 14 (6).
[28] N. Dowling, Mechanical Behavior of Materials, Pearson Prentice Hall, 2007, Ch. Chapter 9: Fatigue of Materials.
[29] H.-K. Joo, T. Sapsis, Performance measures for single-degree-of-freedom energy harvesters under stochastic excitation, J. Sound and Vibration 313 (2014) 4695–4710.
[30] C. McInnes, D. Gorman, M. Cartmell, Enhanced vibrational energy harvesting using nonlinear stochastic resonance, J. Sound and Vibration 318 (2008) 655–662.
[31] D. A. Barton, S. G. Burrow, L. R. Clare, Energy harvesting from vibrations with a nonlinear oscillator, Transactions of the ASME-L-Journal of Vibration and Acoustics 132 (2) (2010) 021009.
[32] M. F. Daqaq, Transduction of a bistable inductive generator driven by white and exponentially correlated gaussian noise, J. Sound and Vibration 330 (11) (2011) 2554–2564.
[33] M. F. Daqaq, Response of uni-modal dung-type harvesters to random forced excitations, J. Sound and Vibration 329 (2010) 3621.
[34] R. Langley, A general mass law for broadband energy harvesting, J. Sound and Vibration(2014) In Press.
[35] R. Harne, K. Wang, A review of the recent research on vibration energy harvesting via bistable systems, Smart Materials and Structures 22 (2) (2013) 023001.
[36] E. Halvorsen, Fundamental issues in nonlinear wideband-vibration energy harvesting, Physical Review E 87 (4) (2013) 042129.
[37] P. L. Green, E. Papatheou, N. D. Sims, Energy harvesting from human motion and bridge vibrations: An evaluation of current nonlinear energy harvesting solutions, J. Intelligent Material Systems and Structures 24 (12) (2013) 1494–1505.
[38] J. Kluger, Nonlinear beam-based vibration energy harvesters and load cells, Master's thesis, Massachusetts Institute of Technology (2014).
[39] J. Kluger, Human motion accelerometer data (June 2014).
URL `http://web.mit.edu/jociek/www/Nonlinear_energy_harvester.html`

List of Figures